CLOUD DETECTION IN NON-POLAR REGIONS FOR CERES USING TRMM VIRS AND TERRA AND AQUA MODIS DATA

Patrick Minnis, Qing Z. Trepte, Szedung Sun-Mack, Yan Chen, David R. Doelling, David F. Young, Douglas A. Spangenberg, Walter F. Miller, Bruce A. Wielicki, Ricky R. Brown, Sharon C. Gibson, Erika B. Geier

Submitted to *IEEE Transactions on Geoscience and Remote Sensing*

January 2008

P. Minnis, D. R. Doelling, D. F. Young, B. A. Wielicki, and E. B. Geier are with the Science Directorate, NASA Langley Research Center, Hampton, VA 23681-0001 USA (email:Patrick.Minnis-1.nasa.gov)
Q. Z. Trepte, S. Sun-Mack, Y. Chen, D. A. Spangenberg, W. F. Miller, S. C. Gibson, and R. R. Brown are with Science Systems and Applications, Inc., Hampton, VA 23666 USA.

Abstract – Objective techniques have been developed to consistently identify cloudy pixels over non-polar regions in multispectral imager data coincident with measurements taken by the CERES on the TRMM, *Terra*, and *Aqua* satellites. The daytime method uses the 0.65, 3.8, 10.8, and 12.0-µm channels on the TRMM Visible and Infrared Scanner (VIRS) and the *Terra* and *Aqua* MODIS. The VIRS and *Terra* 1.6-µm channel and the *Aqua* 1.38 and 2.1-µm channels are used secondarily. At night, the primary radiances are from the 3.8, 10.8, and 12.0-µm channels. Significant differences were found between the VIRS and *Terra* 1.6-µm and the *Terra* and *Aqua* 3.8-µm channels' calibrations. Cascading threshold tests are used to produce clear or cloudy classifications that are qualified according to confidence levels or other conditions, such as sun glint, that could affect the classification. The initial infrared threshold test classifies ~43% of the pixels as clouds. The next level seeks consistency in three (two) different channels during daytime (nighttime) and accounts for roughly 40% (25%) of the pixels. The third tier uses refined thresholds to classify remaining pixels. For cloudy pixels, ~4% yield no retrieval when analyzed with a cloud retrieval algorithm. The techniques were applied to data between 1998 and 2006 to yield average non-polar cloud amounts of ~0.60. Averages among the platforms differ by < 0.01 and are comparable to surface climatological values, but roughly 0.07 less than means from two other satellite analyses, primarily as a result of the algorithm's inability to detect small sub-pixel and thin clouds.

Index terms – cloud detection, cloud, MODIS, VIRS, CERES, cloud mask.

I. INTRODUCTION

Simultaneous measurement of the radiation and cloud fields on a global basis has long been recognized as a key component in understanding and modeling the interaction between clouds and radiation at the top of the atmosphere, at the surface, and within the atmosphere. The NASA Clouds and Earth's Radiant Energy System (CERES) Project [1] began meeting this need in 1998 with the launch of its first broadband shortwave and total band scanners along with the Visible Infrared Scanner (VIRS) on the Tropical Rainfall Measuring Mission (TRMM) satellite in late 1997. During late 1999 and early 2002, the *Terra* and *Aqua* satellites, respectively, were launched with instrument packages that included two CERES scanners each and the Moderate Resolution Imaging Spectroradiometer (MODIS). Together, those satellites have been providing the most comprehensive global characterization of clouds and radiation to date. CERES was designed to fly with high-resolution imagers so that the cloud conditions could be evaluated for every CERES measurement. The cloud properties, specifically, cloud fraction, phase, temperature, height, optical depth, effective particle size, and condensed/frozen water path, are key parameters needed to link the atmospheric radiation and hydrological budgets. Among other applications, they are essential for selecting the proper anisotropic directional models [2] used to convert the CERES radiances to the shortwave albedo and the longwave fluxes needed to define the radiation budget (ERB) at the top of the atmosphere (TOA). Cloud and aerosol properties coincident with broadband radiation measurements are also necessary for sorting out the direct and indirect effects of aerosols on climate. In summary, the combined datasets are critical to understanding the impact of clouds on the ERB at the surface and on the radiative heating profile within the atmosphere. By combining the broadband fluxes with cloud and aerosol properties determined in a radiatively

consistent manner, the CERES dataset should provide an unprecedented set of constraints for climate model assessment and improvement.

The CERES program planned, from its inception [3,4], to analyze coincident imager data to obtain cloud and aerosol properties that could be precisely matched with the CERES scanner fields of view. To obtain a dataset useful for studying climate trends, it was recognized that the above cloud and radiation fields must be determined using consistent algorithms, auxiliary input (e.g., atmospheric temperature and humidity profiles), and calibrations across platforms to minimize instrument- and algorithm-induced changes in the record. By combining the precessing orbit TRMM data with the late morning *Terra* and early afternoon *Aqua* observations, CERES would measure the complete diurnal cycle of clouds and radiation for the Tropics and obtain unprecedented sampling of those same fields in the extra-tropics. Because of the requirements for consistency, simultaneity, and collocation between the cloud and radiation measurements, it was necessary to develop a set of algorithms and a processing system independently of other global cloud processing systems that were either operating or being developed prior to launch of the first CERES-bearing orbiter. The International Satellite Cloud Climatology Project (ISSCP) has been deriving cloud properties from geostationary and NOAA polar-orbiting satellites since 1983 [5], but its products could not be used because ISCCP samples the imager data at an effective resolution of ~32 km (larger than a CERES footprint), cloud particle size is assumed in the retrievals, and simultaneity with the CERES satellites is very limited. The MODIS Atmosphere Science Team (MAST) also planned to derive pixel-level cloud properties from the MODIS data [6,7], but employed algorithms that used many of the 36 MODIS spectral bands and auxiliary input data that are not necessarily consistent over time. The MAST algorithms, which have been used to generate the MOD06 and MOD35 products [8], precluded the use of the VIRS because it

is limited to five channels and would not be able yield cloud properties consistent with the MOD06 and MOD35 results. Furthermore, CERES requires complete cloud information for each footprint and that is not always available in the MOD06 products.

Although the failure of the TRMM CERES scanner early in the mission obviated some of the consistency requirements, other more important factors necessitated the development of independent cloud and aerosol analysis algorithms. CERES is an end-to-end processing system with cloud properties feeding into subsystems that determine TOA, surface, and atmospheric radiative fluxes, including a complex, time-space averaging subsystem that employs geostationary satellite measurements [1]. The cloud detection and retrieval algorithms had to be responsive to the needs of the downstream processing systems and had to be as consistent as possible with the CERES geostationary satellite data processing system [9]. Given the limitations of external cloud datasets and the internal team interaction and consistency requirements, a unique set of cloud detection and retrieval algorithms were developed for CERES utilizing as few channels as possible while producing stable and accurate cloud properties. This paper provides an overview of the algorithms used to detect clouds in non-polar regions. It is the first of a series of four papers [10-12] that describe the CERES cloud analysis system for VIRS Edition 2 (Ed2), *Terra* Edition 2, and *Aqua* Edition 1 (Ed1).

II. DATA

The input data used in the CERES cloud detection algorithms consists of the imager radiances and fixed and variable ancillary information.

A. Satellite Radiances

1) VIRS: The TRMM VIRS is a five-channel imager that measures radiances at 0.65 (visible, VIS), 1.61 (near-infrared, NIR), 3.78 (shortwave-infrared, SIR), 10.8 (infrared, IR), and 12.0 (split window, SW) μm with a nominal 2-km spatial resolution [13]. Table 1 lists the VIRS and MODIS channels available to CERES. For simplicity, unless otherwise noted, the CERES reference channel numbers will be used throughout this paper to refer to a given wavelength. The VIRS cross-track scan extends out to a viewing zenith angle VZA (θ) of 48° and, from the 35° inclined-orbit, yields coverage roughly between 38°N and 38°S. The TRMM orbit gives the VIRS a viewing perspective distinctly different from either geostationary or Sun-synchronous satellites. It samples all local times of day over a 45-day period. At the Equator, this sampling is evenly distributed over the period, but, at higher latitudes, the views are primarily in darkness for roughly 2 weeks followed by 2 weeks of sunlight. The CERES shortwave and total broadband scanners have a nominal field of view size of ~10 km. The VIRS data were obtained from the NASA Langley Distributed Active Archive Center.

Version-5a VIRS data are analyzed by CERES at full resolution. The Version-5a VIRS VIS SIR, IR, and SW channel calibrations appear to be quite stable [14-16], but there is a slight day-night calibration difference in the IR and SW channels that is not taken into account here [15]. The VIRS NIR channel suffers from a thermal leak at 5.2 μm that is corrected using an updated version [17] of the Ignatov and Stowe correction [18]. Although no other calibration problems were revealed in initial studies [19,20], they did not examine the absolute calibration of the channel. Other investigations of the VIRS NIR channel indicated that its gain was too low by ~0.17 compared to other data and theoretical computations using cloud microphysical models [14, 21].

The MODIS and VIRS 1.6-μm channels have similar spectral bands and, therefore, should produce similar reflectances for the same scene. To further investigate the apparent 17% calibration discrepancy, the *Terra* MODIS and VIRS NIR channel radiances were matched and intercalibrated as in [16] using data taken over ocean from every other month from March 2000 through March 2004 when Version 5a ended. Figure 1 shows scatter plots with linear regressions for matched data from two of those months. The VIRS radiances were normalized to the MODIS solar constant of 75.05 $Wm^{-2}sr^{-1}\mu m^{-1}$. The slopes of the fits are 1.209 and 1.177 for March and September 2001, respectively. Overall, the slopes ranged 1.163 in November 2003 to 1.232 with a mean value of 1.193 and the mean offset was 0.0 $Wm^{-2}sr^{-1}\mu m^{-1}$. No significant trends were detected during the 4-year period. A small portion of the differences in the gains may be due to the slight differences in the spectral response functions, but the majority of the discrepancy is due to underestimation of the radiances by the VIRS calibration. The 1.17 correction factor applied to the VIRS NIR channel during the CERES processing should have taken care of much of the calibration bias. Although the TRMM CERES scanner failed after August 1998 and was resuscitated for 1 month, March 2000, the TRMM Ed2 CERES cloud products were also generated from VIRS data taken from January 1998 through July 2001. VIRS continues to operate as of this writing.

2) MODIS: Terra MODIS [22] began collecting data starting in late February 2000 from a Sun-synchronous orbit with a 1030-LT equatorial crossing time. *Aqua* MODIS became operational in July 2002 from a Sun-synchronous orbit with a 1030-LT equatorial crossing time. CERES ingests a 19-channel subset of the 36-channel MODIS complement (Table 1) with the intention of using additional channels in future editions of the algorithms and in other subsystems besides the cloud codes. The 0.25-km channel-1 (0.645 μm) pixels corresponding to the 1-km

channel-1 pixels are also included in the ingested data for future use. The 1-km MODIS data are sampled every other pixel and every other scan line to reduce processing time. This subsetted dataset, provided by the NASA Goddard Space Flight Center Distributed Active Archive Center, was further reduced by sampling every other pixel during actual processing, yielding an effective resolution of 8 km. The CERES-MODIS (CM) *Terra* Ed2 cloud analysis algorithms use the 0.65, 1.64, 3.79, 10.8, and 12.0-μm channels. Because the *Aqua* 1.64-μm channel did not operate properly, the *Aqua* Ed1 non-polar cloud mask used the 2.13-μm channel (CERES reference channel 7) instead. Additionally, the *Aqua* Ed1 algorithms used the 1.38 and 8.5-μm channels to improve thin cirrus cloud detection after finding some obvious deficiencies in the *Terra* Ed2 cloud mask.

The *Terra* VIS channel gain was found to drop by 1.17% after November 18, 2003, but otherwise had no trends. That sudden calibration change is not taken into account in *Terra* Ed2 nor has it disappeared in *Terra* MODIS Collection-5 data. If that decrease is taken into account for all *Terra* data taken after noted date, the trend-free *Aqua* VIS channel gain is 1% greater than its *Terra* counterparts [16]. The *Aqua* reflectance is 4.6% greater, on average, than that from VIRS, a result that is consistent with the theoretical differences between the VIRS and MODIS spectral windows. The gain in the *Terra* 1.64-μm channel was examined for trends using the deep convective cloud method as in [16]. A statistically insignificant decrease in the gain of 0.27% y^{-1} was found from linear regression. It is concluded that the *Terra* 1.64-μm channel calibration is stable during the 6-year period.

The relative calibrations of the *Aqua* and *Terra* 3.79, 10.8, and 12.0-μm channels were examined using the methods of Minnis et al. [15,16]. Figure 2 shows scatter plots of the matched 3.79-μm data taken over the polar regions during August 2004. During daytime (Fig. 2a), the

slope of the linear fit is 1.006 and, on average, the *Terra* SIR brightness temperatures are 0.57 K greater than those from *Aqua*. This result is typical for the period between 2002 and 2006 (Table 2), during which the mean difference is 0.55 K with no trends. At night, data having brightness temperatures $T_b > 250$ K are linearly correlated as during the daytime, but the *Terra* temperatures asymptote to a value of 218 K as the *Aqua* values reach 197 K. This behavior is seen in every month of the intercalibrations indicating a systematic problem with the *Terra* data at night. In the initial VIRS-*Terra* intercalibrations [15], there were too few data points to definitively determine this discrepancy at the low end of the *Terra* temperature range. Thus, the VIRS-*Terra* intercalibrations were repeated for the 2002-2006 period using data from every other month. The nocturnal results are the same as those in Fig. 2b. The large bias in the average SIR brightness temperature differences (BTD) at night for *Terra* and *Aqua* (Table 2) reflect the strong contribution of the colder temperatures to the average because the data were taken over polar regions, while less conspicuous nighttime BTDs for VIRS-*Terra* and VIRS-*Aqua* result from having fewer very low temperatures during the tropical night. During the day, the VIRS SIR brightness temperatures are 1.39 and 0.85 K less than the *Terra* and *Aqua* values, respectively, confirming the 0.55 K bias between *Aqua* and *Terra* SIR daytime data.

The intercalibrations among the three instruments' IR and SW channels are summarized in Table 2. The differences between the *Terra* and *Aqua* 10.8 and 12.0-μm T_b's are slightly larger at night than during the daytime. This difference appears to be the result of somewhat larger *Terra* T_b's at the low end of the range, temperatures that are infrequently observed in the daytime comparisons. This discrepancy at the low end appears to have been eliminated in the MODIS Collection 5 data. Roughly half of the nearly 1 K bias between the VIRS and MODIS SW T_b's can be explained by the differences in the spectral response functions [15]. In the data processing,

spectral differences are taken into account theoretically. Other calibration differences, such as those in Fig. 2, were not corrected prior to analysis because they were not known before the start of the subject CERES Edition processing. To date, the CERES cloud analysis algorithms have been applied to *Terra* and *Aqua* Collection-4 MODIS data through April 2006 and to Collection-5 MODIS data from January 2006 through December 2006.

B) Variable ancillary data

The CERES Meteorology, Ozone, and Aerosol (MOA) dataset includes vertical profiles of temperature, humidity, wind, and ozone and total aerosol amounts. The ozone data, which include the total column concentration, are taken from the 2.5° National Centers for Environmental Prediction (NCEP) Stratosphere Monitoring Ozone Blended Analysis (SMOBA) [23] or from the Earth Probe Total Ozone Mapping Spectrometer (total column optical depth only) at a 1.25° resolution when SMOBA data are not available. The CERES MOA temperature, wind, and humidity profiles are based on numerical weather analyses (NWA): the European Centre for Medium-range Weather Forecasting (ECMWF) reanalyses for VIRS and on the Global Modeling Assimilation Office GEOS 4.03 analyses [24] for the MODIS processing. The ECMWF profiles were available at a nominal resolution of 0.5° every 6 hours and surface skin temperature T_{skin} was available every 3 hours. GEOS profiles and skin temperatures were made available at the same temporal resolutions on a 1° grid. All input MOA data were interpolated to produce, on a common 1° x 1° grid, surface skin temperature, geopotential height, and pressure, total column ozone, and profiles of temperature, specific humidity, and ozone at up to 58 levels from the surface to 0.1 hPa [25].

Daily ice and snow extent data were obtained from the Near Real-Time SSM/I EASE-Grid Daily Global Ice Concentration and Snow Extent products [26] on a nominal 25-km polar

stereographic grid and supplemented by the NESDIS Interactive Multisensor Snow and Ice Mapping System Daily Northern Hemisphere Snow and Ice Analysis in the vicinity of coastlines [27]. All snow and ice extent values were interpolated to a 10' grid.

For land and snow surfaces, monthly updated VIS overhead-sun clear-sky albedos,

$$\alpha_{cso1}(\lambda, \phi) = \alpha_{cs1}(\lambda, \phi; \mu_o=1), \quad (1)$$

were derived on a 10' grid from VIRS and MODIS 0.64-μm data along with overhead-sun NIR surface albedos $\alpha_{si}(\lambda, \phi; \mu_o=1)$ for channels 2 and 7 from VIRS and *Terra* MODIS 1.64-μm data and from the MODIS 2.13-μm data using clear-sky values from earlier versions of the CERES processing system [12,28]. The latitude and longitude are indicated by λ and ϕ, respectively, while μ_o = cos(SZA) and SZA is the solar zenith angle. These albedos are used with angular directional models, and, for the NIR channels, with approximations for atmospheric absorption to estimate the clear-sky reflectance for a given scene. From the overhead-sun albedos, the VIS clear-sky albedo is estimated at a given SZA for any 10' region as

$$\alpha_{cs1}(\lambda, \phi; \mu_o) = \delta_{cs1}(K(\lambda, \phi); \mu_o)\ \alpha_{cso1}(\lambda, \phi), \quad (2)$$

where δ_{cs1} is normalized directional reflectance model that predicts the variation of the clear-sky albedo with SZA for a given surface type K, which is one of the 19 modified International

Geosphere Biosphere Programme (IGBP) surface types [29]. Similarly, the NIR surface albedo at a given SZA for any 10' region is estimated as

$$\alpha_{si}(\lambda, \phi; \mu_o) = \delta_{si}(K(\lambda, \phi); \mu_o)\ \alpha_{soi}(\lambda, \phi), \quad (3)$$

where i indicates either channels 2 or 7 and the subscript o denotes overhead sun conditions. Values of the directional reflectance models and their derivation can be found in Sun-Mack et al. [12] for all surfaces except snow and water, where the updated model of Minnis and Harrison [30] is employed.

The VIS clear-sky reflectance is estimated as

$$\rho_{cs1}(\lambda, \phi; \mu_o,\mu,\psi) = \alpha_{cs1}\ \chi_{VIS}(K; \mu_o,\mu,\psi), \quad (4)$$

where χ_{VIS} is the VIS bidirectional reflectance distribution function (BRDF), μ = cos(VZA), and ψ is the relative azimuth angle. For the NIR channels, 2 and 7, the predicted clear-sky reflectance is,

$$\rho_{csi} = \alpha_{si}\ \chi_{si}\ (K; \mu_o,\mu,\psi)\ t_i, \quad (5)$$

where χ_{si} is the NIR BRDF and t_i is the combined transmittance of the atmosphere to the downwelling and upwelling beam for channel i [28]. The VIS BRDFs are taken from Minnis and Harrison [30] for water surfaces (K= 17) and from Suttles et al. [31] for land and coast (K= 1-14, 18, 19), snow (K = 15), and desert (K=16). The theoretical snow BRDF described by Sun-Mack et al. [28] is employed for the MODIS analyses. The VIS BRDF model of Minnis and Harrison [30] was also used for the NIR channels over water surfaces. BRDFs from Kriebel [32] were used for the NIR channels over most land surfaces as described in [28], while the broadband desert model of Suttles et al. [31] was used for the NIR for deserts and the theoretical models described in [28] were used for snow and ice surfaces.

Uncertainties were computed from the same data base used to determine the clear-sky and surface albedos [28]. Nominally, the relative rms average $\sigma_{cs1}(\lambda,\phi,m)$ of the temporal and spatial standard deviations of the mean $<\alpha_{cso1}(\lambda, \phi,m)>$ of $\alpha_{cso1}(\lambda, \phi)$ were computed for each month m using daily pixel-level data from the earlier editions of the VIRS and *Terra* MODIS analyses. These values were normalized to $<\alpha_{cso1}(\lambda, \phi,m)>$ to obtain the basic uncertainty in the monthly mean overhead sun albedos. The resulting uncertainties were filtered to eliminate values from poorly sampled areas where mostly cloudy conditions prevailed during the month. The filtered data were then averaged for each surface type to obtain $<\alpha_{cso1}(K,m)>$ and $\sigma_{cs1}(K,m)$. These surface type averages were then used to fill in uncertainty values for each region of the given surface type that had no results for the month. When the final edition processing took place, these uncertainties were replaced with default values whenever the nominal value was less than the default value. A similar process was used for channels 2 and 7.

Spectral surface emissivities $\varepsilon_{Si}(K, \lambda, \phi)$ at the 10' are used in conjunction with the reanalysis skin temperatures to estimate the clear-sky radiances for the CERES reference channels, i = 3,6,

where the wavelengths are listed in Table 1. The values of surface emissivity are taken from the results of Chen et al. [33, 34]. During daytime, solar radiation in the SIR channel is reflected by the surface in addition to the thermal emission from the surface. To account for this reflected contribution, the SIR or channel-3 surface reflectance is estimated as

$$\rho_{cs3} = (1-\varepsilon_{S3})\, \chi_{s7}\, (K;\, \mu_o, \mu, \psi)\, t_3, \qquad (6)$$

The BRDFs used for the 2.13-µm channel are also used for channel 3 because of the lack of bidirectional reflectance measurements at the SIR wavelengths. An exception is the theoretical 3.8-µm snow reflectance model [28], which is used here for all snow and ice surfaces.

Figure 3 shows an example of the global maps of monthly mean surface emissivities and overhead-sun albedos for *Terra* MODIS. Note, areas with permanent snow or ice cover or have seasonally persistent snow cover are given albedos for snow-covered scenes. Where the snow cover is highly variable, the albedos are initialized with the snow-free value and can vary during a given month. Figure 3a shows that some areas with seasonal snow cover have the average snow albedos while other areas that are typically snow covered during January have the snow-free albedos. In practice, these snow-free albedos are overwritten during processing with the model snow albedos from the model whenever the ice-snow map indicates snow cover for the area. Variations in the emissivity and albedo patterns are generally related. The desert VIS albedos (Fig. 3a) are typically higher than those for no-snow surfaces but are less than their 1.64-µm counterparts (Fig. 3b). The surface emissivities decrease with increasing VIS albedo, except over

snow-covered regions. Surface emissivity at 3.8-μm (Fig. 3c) is typically less than that at 10.8 μm (Fig. 3d). A few ε_{S3} values over the western Sahara are as low as 0.60 compared to 0.92 for ε_{S4}.

C) Fixed ancillary data

Average land elevation was determined for each 10' region from the 1-km United States Geophysical Survey (USGS) GTOPO30 dataset (http://edc.usgs.gov/products/elevation/gtopo30/gtopo30.html). The surface type for a given 10' region is taken from the modified IGBP map described by [28]. The percentage of water surface in a given 10' region was determined from the 1-km IGBP dataset.

III. METHODOLOGIES

The CERES scene classification is one of the two main parts of the CERES cloud processing system, which is shown schematically in Fig. 4. To define a pixel as cloudy or clear (cloud mask), the system ingests the radiance and ancillary data described above on a pixel tile basis. Each tile consists of an array of pixels defined by 8 scan lines and 16 elements. For VIRS and MODIS, these arrays nominally correspond to 16 km x 32 km and 32 km x 32 km, respectively. Although each pixel is analyzed individually, all pixels within a given tile use the same predicted clear radiances and atmospheric corrections in the retrieval. After ingesting the input data, the expected clear-sky radiances and clear-cloudy thresholds for the tile are computed for each channel and the observed radiances are compared to the thresholds to determine if each pixel within the tile is clear or cloudy. If cloudy, the pixel is passed to the retrieval subsystem (shaded boxes) where cloud properties are determined. If no valid results can be obtained, the pixel is given a no-retrieval classification and tested within that system to determine if it warrants a clear classification. If categorized as clear in the original mask, the pixels may be used to update the

clear radiance map for a given 10' region and then are passed into the cloud property retrieval subsystem along with any cloudy pixels from the same tile. The predicted clear-sky radiances for the tile are also passed into the retrieval subsystem. These processes are described in detail below.

A. Clear-Sky Radiance Prediction

To compute expected clear-sky radiances, the surface emissivities, skin temperatures, atmospheric profiles, and albedos must be defined for the tile. To define the tile skin temperatures and atmospheric profiles of temperature and humidity, the code determines which NWA grid box has its center closest to the tile center. The 6-hourly profiles and 3-hourly skin temperatures for that box are then linearly interpolated to the time of the satellite measurement to provide input for the clear-sky radiance and atmospheric correction calculations. Average clear-sky VIS albedos, NIR surface albedos, surface elevation, surface emissivities, water percentage, snow coverage, and albedo-weighted BRDF factors are computed using values of each parameter for all 10' regions with centers that fall within the perimeter of the tile. The dominant surface type is also identified. Similarly, the largest average 10' rms uncertainty in the box is identified for each channel. Unless otherwise noted, these average values are used hereafter in the discussion of the clear-sky radiance prediction or mask analyses.

1) Visible and near-infrared: The channel-1 and NIR clear-sky reflectances for each pixel are computed as in (4) and (5), respectively, using the values for χ and α corresponding to the 10' region containing the given pixel. No atmospheric corrections are applied to the VIS reflectances. The atmospheric transmittance for 1.62-μm channel is estimated as

$$t_2 = \exp[-\tau_2(1/\mu_o + 2.04)], \quad (7)$$

where τ_2 is the effective water vapor optical depth parameterized as a function of column precipitable water based on fits to adding-doubling radiative transfer computations

2) Shortwave infrared: The SIR radiance leaving the surface is approximated as

$$B_3(T_{s3}) = \varepsilon_3 [B_3(T_{skin})] + \alpha_3 (L_{a3} + \chi_3 S_3'), \quad (8)$$

where B_3 is the Planck function evaluated at the energy-equivalent wavelength of the channel-3 band, T_{s3} is the apparent surface temperature at 3.8 μm, L_{a3} is atmosphere-emitted downwelling radiance and S_3' is the solar radiance incident at the surface. The SIR surface albedo is estimated as

$$\alpha_3 = 1 - \varepsilon_3. \quad (9)$$

The incident solar radiation at the surface is computed as

$$S_3' = \mu_o \sum_{m=1}^{5} S_{om} \Delta\lambda_m \prod_{n=19}^{1} t_{d\,3mn}, \quad (10)$$

where S_{om} is the TOA solar radiance for wavelength interval m, where m denotes the 0.1-μm-wide sub-bands 1 through 5 for the SIR channel between 3.55 and 4.05 μm. The transmittances for each layer n to downwelling radiation t_{d3mn} are computed using the correlated k-distribution

method [35] and the same coefficients employed by [15]. These coefficients include N_2O absorption, which was not in the original set of coefficients [35]. The value of L_{a3} is estimated as the integral of the radiation emitted by each layer transmitted to the surface over all five sub-bands. Those calculations use the temperature and humidity profiles from the NWA interpolations. Those profiles are sometimes adjusted with the technique of Rose et al. [36] to ensure consistency between the observed and computed radiances. It is assumed that the surface emissivity is constant across all five sub-bands.

The upwelling SIR radiance at the surface $B_3(T_{s3})$ is then corrected for attenuation by the atmosphere to predict the clear-sky temperature T_{cs3}. Different sets of transmittances are computed for the upwelling radiation as a function of the pressure at the radiating surface to account for band saturation. This approach yields a mean difference between the observed and predicted values of T_{cs3} of –2 to +2K and –1 to +1 K during daytime and nighttime, respectively, with standard deviations σ_3 less than 3K and 2K.

3) Infrared: The 10.8 and 12.0-μm TOA clear-sky temperatures, T_{cs4} and T_{cs5}, respectively, are derived in a manner similar to that for channel 3, except without the solar radiance contributions. Again, the correlated *k*-distribution method is applied to the adjusted 3-hourly skin temperatures computed by a numerical weather analysis model and corrected for temporal phase lags and the surface emissivity, then adjusted to the TOA by accounting for gaseous absorption and emission of the atmosphere. Channel-3 clear-sky temperature uncertainties are estimated as the standard deviations between the predicted and observed temperatures with minima of 2.5 and 3.0 K for ocean and land, respectively. The nominal 10.8-μm uncertainty, $\sigma'_{cs3}(\lambda,\phi,m)$, is given in Kelvins and is adjusted as a function of VZA to account for increases in apparent optical depth with rising VZA. The resulting uncertainty used in the clear-sky threshold is

$$\sigma_{cs3}(\lambda,\phi,m) = \sigma'_{cs3}(\lambda,\phi,m) + delT(\mu), \quad (11)$$

where $delT = 0$ if $\mu = 1$ or if $\mu < 1$,

$$delT = 4.11 - 7.69\,\mu + 3.57\,\mu^2. \quad (12)$$

B. Non-polar Scene Identification

The CERES cloud mask consists primarily of cascading threshold tests. To define a pixel as cloudy, at least, one of its five spectral radiances must differ significantly from the corresponding expected clear-sky radiances. A cloudy pixel may be classified as strong or weak depending on how much the radiances differ from the predicted clear-sky radiances. Pixels identified as clear are designated as weak or good or categorized as being filled with smoke, fire, or aerosol, contaminated by sun glint, or covered with snow. These qualifiers for the basic classifications are valuable provide information for assessing the certainty of the retrieval or for explaining why the classification may differ from expected values. For VIRS, the daytime ($SZA \leq 82°$) masking algorithm can use all five channels, while the nighttime technique only employs channels 3, 4, and 5. A few extra channels are used for the MODIS processing (see Table 1). Polar regions are defined as all areas poleward of 60° latitude and all areas between 50° and 60° latitude where the snow-ice maps indicate the surface is covered with snow or ice. The non-polar masks apply to all other areas. Although the cascade logic and some of the tests to discriminate clear from cloudy pixels are different, much of the theoretical basis and details of some tests are given by Baum et al. [37].

1) Daytime: Every non-polar pixel is classified during daylight using a sequence of tests as outlined in Fig. 5. The first check, or **A** test, identifies all pixels that are obviously too cold to be cloud free. If $T_4 < T_{lim}$, then the pixel is designated a strong cloud. For VIRS Ed2, this test was called without restrictions and the value of T_{lim} is equal to the temperature at 500 hPa over land or to 260 K over ocean. In the MODIS processing, the test is not used if $T_{skin} < 270$ K or the surface elevation exceeds 4 km.

If the pixel is not cloudy after the **A** test, it is then compared against the expected clear-sky radiances in the following **B** tests, where the parameters *B1*, *B2*, and *B3* are initialized to 0.

$$\text{If } T_4 < T_{cs4} - \sigma_{cs4}, \qquad B1 = 1. \tag{13a}$$

$$\text{If } \rho_1 > \rho_{cs1}\,(1 + \sigma_{cs1}), \qquad B2 = 1. \tag{13b}$$

$$\text{If } BTD_{34} > BTD_{cs34} + \sigma_{cs34}, \qquad B3 = 1. \tag{13c}$$

In these equations, the subscript numbers refer to channel number and the subscript *cs* denotes the predicted clear-sky value. When two channels are indicated, the parameter is either the ratio of or the difference between the two channels, e.g., BTD_{34} is the observed brightness temperature difference between channels 3 and 4. If the sum of the **B** parameters is 0 or 3, then the pixel is initially identified as good clear or cloudy. If certain conditions are met, the pixel may be reclassified after passing through a set of **ALL B** clear or cloudy tests detailed in Fig. 6. The former checks spectral consistency in glint-free or sun glint conditions over ocean using sun glint probability (SGP) or tests for shadows over land (Fig. 6a), while the latter checks for other

effects on the assumed thresholds as a result of sun glint or highly reflective desert surfaces (Fig. 6b). These **ALL B** tests use a variety of parameters including observed reflectance ratios, $R_{ij} = \rho_i / \rho_j$ and constraint reflectance ratios r_{ij}, where i and j are channel numbers. The constraints are defined for sun glint, indicated with the subscript g and other conditions denoted by the subscript c. For *Aqua*, channel 7 is used instead of channel 2. These defining reflectance ratio values are listed in Table 3. The initial **B** result is the final classification unless the **ALL B** tests change it. If the sum of the **B** parameters is either 1 or 2 (Fig. 5), then a thin cirrus test is applied (*Aqua* Ed1 only) followed by one of six sets of **C** tests that depends on which **B** tests failed and on the surface type. The *Aqua* thin cirrus test is shown in Fig. 7. These tests utilize the 1.38-µm reflectance ρ_8 and the 8.55-µm brightness temperature in the form of BTD_{64}, as well as BTD_{45}. Several constraint parameters are used that depend on the precipitable water vapor, which is indicated by the subscript, *PW*. A cruder version of the thin cirrus test was applied in some of the **C** tests for all satellites.

The **C** tests adjust the clear-sky uncertainties and may also involve channels 2 or 5 in addition to the three channels used in the **B** tests. For example, if the scene is bright and cold over land, the **C** test will check for snow using the expected snow reflectance ratio R_{21} of 0.65-µm to 1.6 µm. From these **C** tests, a pixel categorized as clear may be assigned additional classifiers such as strong, weak, snow, aerosol, smoke, fire, or glint. Cloudy pixels may be classified as good, weak, glint, or multilayered. Figure 8 shows one of the six **C** tests, **C1**, which is called when the IR test fails ($B1 = 0$). Over land (Fig. 8a), the VIS and BTD_{34} threshold are relaxed by a factor of 2 and by a variable relaxation factor, f_r, respectively. The value of f_r is 2.0 for desert areas and 1.5 for vegetated land areas. If both tests are passed, the results are tested for snow using a temperature and reflectance ratio tests. If positive snow does not result, the pixel is

classified as weak or good cloud depending on the temperature and the reflectance ratio, R_{21}. If only the VIS test is passed, the radiances are tested for snow. If no snow, then a test for smoke is applied by further increasing the VIS threshold. If no smoke is detected, then the pixel is classified as weak or good cloud. Similarly, if only the BTD_{34} test is passed, then the cloud is classified as weak or good depending on R_{21}. If both tests fail, then the radiances are examined to determine if the pixel should be classified as clear good, weak, smoke or fire.

Over ocean (Fig. 8b), the SGP is tested to determine if there is any likelihood of sun glint affecting the clear reflectances. If SGP exceeds 40%, then the sun glint tests listed in Fig. 9 are applied. The clear sun glint tests rely on the spectral reflectance ratio R_{31}, the VIS reflectance and the IR or SIR temperatures. The cloud tests depend on T_4 and BTD_{34}. The latter is compared to the sum of two uncertainties: the BTD_{34} sun glint uncertainty,

$$\sigma_{cs34g} = 4.316 \text{ K} + 0.123 \text{ K SGP}, \qquad (14)$$

and the nighttime high-cloud BTD_{34} uncertainty, σ_{cs34hi}. The latter is simply the daytime uncertainty with the reflectance components removed. If the sun glint tests fail for the strong sun glint cases (Fig. 8b), then a final test is applied using two spectral reflectance ratios. When SGP falls between 2 and 40%, moderate sun glint tests are invoked using looser BTD_{34} and VIS reflectance uncertainties. Again, spectral reflectance ratios are used to determine a classification. For non-glint cases, SGP < 2%, a set of tests are applied to determine if aerosols can be causing the enhanced reflectances. Reflectance ratios, T_4, and an enhanced BTD_{34} uncertainty are used to detect aerosols. If the aerosol tests are not passed, then the thresholds for VIS and BTD_{34} are enhanced and applied in fashion similar to that for the land cases. The pixel is good cloud only if

both tests are passed. Because of the obvious complexity of the **C** tests and the number of required diagrams, only **C1** is illustrated here. More detail as well as the flowcharts for the remaining five **C** tests (**C2 – C6**) are provided elsewhere (http://www-angler.larc.nasa.gov /CERES_algorithms/).

An example of predicting the clear-sky VIS reflectances for the daytime mask is shown in Figure 10 for data taken around 17 UTC on 21 December 2000 over the southwestern USA and northern Mexico. The 3-channel *Terra* MODIS image (Fig. 10a) shows green and bluish areas that are clear land and desert. Dark areas are clear water, while white, grey, pink, and yellow areas correspond to clouds. The bright magenta areas are covered with snow. Some of the input data, radiances, water percentage, snow/ice, and clear-sky overhead albedo, are represented in Figs. 10a-10d, respectively. The computed directional reflectance model values (Fig. 10e) applied to the overhead-sun albedos yield the clear-sky albedos at the image time (Fig. 10f). These are multiplied by the BRDF factors (Fig. 10g) to obtain the predicted clear-sky VIS reflectances (Fig. 10h). When compared to the observed VIS reflectance in Fig. 10i, it is apparent that in areas where it is visually cloud or snow-free, ρ_{cs1} is reasonably close to the observed value.

The corresponding processes for estimating T_{cs4} and BTD_{cs34} are illustrated in Fig. 11. The MOA skin temperatures (Fig. 11b) are given at the 1° scale and used with the MOA temperature and humidity profiles (PW in Fig. 11c illustrates the variability in humidity) and the surface emissivities (Figs. 11d and 11g) taken from maps like those in Figs. 4c,d to compute the clear-sky brightness temperatures. The values of T_{cs4} in Fig. 11e were computed at the tile scale and tend to be less than the observed values (Fig. 11f) over land and slightly higher over water. This difference can mostly be attributed to the MOA skin temperatures since they are typically less

than the observed clear-sky temperatures even before the surface emissivity and atmospheric corrections reduce T_{skin} to T_{cs4}. The values of BTD_{34} (Fig. 11h) are greater than the observed values (Fig. 11i) in some clear areas and less than the values in other areas. The observations do not show the same degree of VZA dependence over water that is predicted.

Using these clear-sky values in the daytime cloud mask yields the results shown in Fig. 12. The **ABC** summary (Fig.12a) shows examples of the various tests that were used to classify the clouds. While a few snow-covered regions are shown in yellow because the pixels passed **B1** and **B2**, most are blue having passed only **B2** because T_{cs4} is less than T_4 (Fig. 11e-f). A large part of the desert and shadowed areas passed **B1**, but failed the other two. Only a few areas of high clouds passed the **A** test (white), while many of the clouds over the Rocky Mountains and the Gulf of Mexico passed all three **B** tests (gray). The other colors indicate the final tests used to classify the pixels.

The cloudy pixels (Fig. 12b) are identified as good (white), weak (pink), or no retrieval (blue). The last category indicates those pixels that were identified as cloudy have radiances that cannot produce solutions to the models used in the cloud retrieval program [11]. Typically, no-retrieval cloudy pixels are reclassified as clear in the cloud retrieval portion of the system using an additional mask developed by Welch et al. [38]. The clouds over the snowy areas and over the southeastern part of the image appear to be properly classified when compared with the composite image in Fig. 11a. The cloudy areas over northeastern Mexico, southern Texas, and near the Arizona-New Mexico border are difficult to see in Fig. 11a, but they appear as relatively cold areas in Fig. 11f and as warmer areas (larger BTD_{34}) in Fig. 11i. Those characteristics are typical of thin cirrus clouds. Weak clouds are detected near the thin cirrus clouds and over the Pacific and Sea of Cortez where the clouds are very faint in the image. The no-retrieval pixels

occur along the edges of the snowy areas and the thin cirrus regions. Although some likely clear pixels along the snow field edges are misclassified as good clouds, overall, the mask (Fig. 12c) appears to correctly identify most pixels.

The resulting clear pixels (Fig. 12d) are classified as weak (light green), good (dark green), aerosol (pink), and snow (white). The gray areas correspond to clouds. The clear areas are mostly good. Some shadowed pixels are identified over Louisiana (center right) next to the cloud edges. The snow-covered areas correspond roughly to those in the snow map (Fig. 10b), but some additional areas are added east of the western section and around the northwestern and southern edges of the eastern section. Much additional detail is resolved relative to the snow-map snow areas and some snowy parts in Fig. 10b are reclassified as good clear, e.g., the region in the northwest corner of the image.

2) Nighttime: The nighttime mask is similar to the daytime cascade of tests. The **A** test (Fig. 13) is followed by **D** tests that begin with $D1 = D2 = D3 = 0$. The **D1** and **D2** tests are the same as **B1** and **B3**, respectively. The threshold for the **D2** test, however, uses, the nighttime threshold for high clouds, BTD_{cs34hi}. Because low clouds are often indistinguishable from clear skies at night in channel 4 and BTD_{34} is often negative [39], the **D3** test is used to detect low clouds by checking for smaller-than-expected values of BTD_{34}. In this test, BTD_{34} - BTD_{cs34} is compared to to σ_{cs34lo}, which is equal to 0.5 - BTD_{cs34hi}. If any of the **D** tests passes, then one of the five **E** tests are applied that involve refined thresholds and channel 5 radiances. Otherwise, the pixel is passed on to the **ALL D** clear tests that are applied only in the twilight zone, defined as an area where 82° < SZA < 87.5°. At these high SZA's the reflectance component in channel 3 is often just large enough to offset the negative BTD_{34} seen for low clouds at night, but is not sufficient to

produce a strongly positive value typical of low clouds during the daytime. Thus, the additional tests, outlined in Fig. 14, are invoked. Over ocean, VIS and NIR reflectances that are both significantly greater than the predicted clear sky values will cause the pixel to be reclassified as weak cloud. To be recategorized as weak cloud over land, the observed reflectances must both exceed 0.20 and the BTD_{34} must be outside of the range between -1 and 4 K. If no reclassification occurs, the pixel remains as good clear. Similar to the daytime **C** tests, the **E** tests, applied to the remaining pixels, change the uncertainties to yield strong or weak clear or strong or weak cloudy classifications.

Figure 15 shows the outline of the **E1** test, which is invoked when **D1** and **D2** are both passed. That is, T_4 is lower than expected and BTD_{34} is greater than the expected clear-sky value. The channel-4 and BTD_{34} uncertainties are decreased and increased, respectively. If the observations pass both tests, then the pixel is a good cloud over ocean but undergoes one more test, using BTD_{45}, over land to see if thin cirrus caused the greater-than-expected BTD_{34} value. If only one of the two **E1** tests passes, then, over ocean, the pixel is a weak cloud if the channel-4 test passes and weak clear if BTD_{34} test passes. For land scenes, the thin cirrus (**Ci**) test is applied. This test classifies a pixel as thin cirrus if BTD_{45} exceeds threshold values that depend on VZA and T_4. The threshold values were originally developed by Saunders and Kriebel [40]. The basis for the test and the threshold values are discussed by [36]. If neither **E1** test is passed, the **Ci** test is applied regardless of surface type. As in the case of the **C** tests, only one example of the **E** tests is shown here for brevity. The details of the remaining **E** tests, **E2**-**E5**, can be found elsewhere (http://www-angler.larc.nasa.gov/CERES_algorithms/).

Figure 16 illustrates the results of applying this classification scheme to VIRS data taken over Texas at 6 UTC, 25 March 2001. The three-channel infrared pseudocolor image (Fig. 16a)

renders clear areas in blues and tans and cloudy pixels in colors ranging from gold to white. The 3.7-μm surface emissivity (Fig. 16g) is generally defined only at the 0.5° scale although some 10' regional variability is evident. It tends to increase from the forested eastern areas to the high plains in the west. Figure 16e shows the BTD_{34} values ranging from less than -5 K to more than 20 K. The negative values generally correspond to low clouds while the greater positive values are associated with thin high clouds. Clear areas typically have values near zero. Observed BTD_{45} values are given in Fig. 16f, where low clouds and clear areas have values of $\pm$1 K and high clouds have positive values up to 4 K or greater. The low clouds also tend to have 11-μm temperatures comparable to the clear areas (Fig. 16d). The resulting cloud mask and summary of nighttime tests are depicted in Figs. 16b and c, respectively. The **A** test (white in summary) and the **E1** test (light blue) pick up many of the thick and thin high clouds. The **E3** test (red) detects many of the thinnest cirrus clouds, particularly those around the edges of those detected by the **E1** test. Thicker midlevel and cirrus clouds over low clouds are found using the **E5** test. In those instances, the BTD_{34} values are similar to the expected clear temperature differences. Very low or sub-inversion clouds were classified with the **E2** and **E4** tests. The **ALL D** clear category is indicated in green. Other clear areas were classified with the **E** tests. In some instances, it appears that cloudy pixels were misclassified as clear. These were mainly low clouds that were warm and had BTD_{34} values close to the expected clear levels. They can be seen by comparing the areas where **E** tests were applied with cloudy areas in the CERES mask image. Visually, the results are quite reasonable despite a few missed clouds.

IV. RESULTS AND DISCUSSION

As noted earlier, the CERES non-polar scene identification mask was applied to several years of VIRS data and, along with the CERES polar mask [10], to long periods of *Terra* and *Aqua* MODIS data. A few examples summarizing the results are presented and discussed here.

A. Scene Identification Statistics

Tables 4 and 5 summarize, for day and night respectively, the relative frequency of the various tests that resulted in a final classification for all of the non-polar *Terra* MODIS pixels during March 2000. During daytime (Table 4), the **A** test accounts for nearly 43% of the decisions; more occur over ocean than over land and desert surfaces. The **All B** tests result in a classification for almost 40% of the pixels leaving only 20% to be categorized by the **C** tests. The **All B** clear classification is most common over desert areas, while **All B** clouds occur most frequently over ocean. The channels that are used in each **C** test are noted in the first column of Table 4. The **C5** test, in which only the IR channel indicates clouds, is invoked least often of all of the **C** tests. Bad data are those pixels having out-of-range or saturated radiances in any of the channels used in the mask. They occur mostly over land and account for 1% of pixels overall.

At night (Table 5), the frequency of positive (cloudy) **A** tests is nearly the same as during the daytime, while the **ALL D** clear occurrences are slightly greater than their daytime **ALL B** counterparts. In contrast to daytime, the **E5** test, which is enacted when only the IR threshold is exceeded, is used most often followed by the **E5** and **E3** tests. No bad data are seen in this nighttime dataset, probably because most cases are due to extremely high temperatures or reflectances, which do not occur at night. The day and night cloud mask test statistics vary somewhat from month to month, however, the results in Tables 4 and 5 are fairly typical for both

Terra and *Aqua*. The number of positive **A** tests decreases for VIRS presumably because the proportion of colder clouds drops when the midlatitudes are excluded from the dataset.

Of the pixels initially classified as clear during daytime, roughly 92% are classified as good clear, 4.6% as clear glint, 1.6% as clear snow, 1.4% as weak clear, and the remainder divided between weak clear, shadow, aerosol, and smoke. At night, approximately 80% of the pixels is good clear, 14% is weak clear, and 6% clear snow. In daytime cloudy conditions, ~92% of the pixels is good cloud while around 3% is weak cloud, 1% is glint cloud, and 4% is classified as no retrieval. At night, roughly 98% are good clouds, 1.3% are weak clouds, and 0.5% are no retrievals, occurring mostly during twilight conditions. Roughly half of the no retrieval pixels, which typically occur over bright surfaces like desert, snow, and glint, are reclassified as clear pixels in the retrieval subsystem. The *Terra* March 2000 statistics are typical for all of the *Terra* and *Aqua* non-polar scene classifications. The number of no retrievals from VIRS is slightly smaller, around 3%, presumably because of fewer snowy and strong sunglint conditions.

B. Cloud Amount Distributions and Consistency

The TRMM Ed2 and *Terra* Ed2 cloud amount distributions for March 2000 are presented in Fig. 17. This month is shown because it is the only period when CERES broadband scanners operated on both TRMM and *Terra*. During daytime (Fig. 17a), the VIRS and MODIS results have similar patterns with some distinctive differences. For example, fewer clouds are detected by *Terra* over the Sahara and most land areas, while differences over ocean vary. Over the intertropical convergence zones (ITCZ), the VIRS cloud amounts are greater, but in the southern ocean subtropical subsidence areas, the VIRS cloud cover is slightly less. These discrepancies can arise from a number of factors such as differences in spectral and temporal and VZA

sampling characteristics. Over the Tropics, VIRS samples nearly all local times during a given month, but has divergent sampling patterns in the subtropics and midlatitudes. During March 2000, most of the daytime samples near 32°N were taken in the hours just before sunset and after sunrise, while at the 32°S, VIRS sampled, on average, around 1300 LT. *Terra* MODIS viewed a given area in the VIRS domain within ±1.5 hours of 1030 LT at VZA < 70°. Thus, from a sampling standpoint many of the daytime differences are reasonable.

Similar sampling differences might explain the differences at night (Fig. 17b), except over the Sahara Desert where the cloud amounts from VIRS greatly exceed those from *Terra*. In this instance, the VIRS results are likely an overestimate and may be due to the use of older emissivity maps based on Advanced Very High Resolution Radiometer data [33], to differences in the surface skin temperatures between the ECMWF and GEOS4.03 analyses, or to some slight differences in the *Terra* Ed2 and VIRS Ed2 nighttime masks. Several extra twilight tests and a BTD_{64} nighttime test were added for *Terra* Ed2. At night, the VIRS analysis consistently detected many more clouds than *Terra* over the western Sahara during all months (not shown). The *Terra* processing produces an artifact, a discontinuity at 50°N, not seen in the VIRS, which only views to 38°N. It occurs because of an error in the *Terra* Ed2 polar mask and is discussed by [10].

Many of the latitudinal sampling inconsistencies are diminished somewhat by averaging the VIRS results over periods of 3 months or so. Figure 18 shows the combined cloud amounts derived from VIRS and *Terra* for summer 2000 (June, July, August; JJA), and winter 2000-2001 (December, January, February; DJF). During daytime (Fig. 18a), the VIRS zonal mean cloud amounts are systematically larger than those from *Terra* except south of 30°S. The VIRS and *Terra* cloud fractions are in closer agreement during the night (Fig. 18b) except over the northern

subtropics, particularly at the latitudes (15°-32°N) corresponding to the Sahara Desert. It is clear that the main source of the discrepancy at those latitudes is due to the differences over land, which peak at 0.11 around 22.5°N (Fig. 18c). Over ocean, the mean zonal differences (VIRS-MODIS) vary between -0.025 and 0.025. Overall, the zonal differences range from -0.03 to 0.05. Not all of the differences are due to changes between the VIRS and *Terra* processing in the numerical weather analyses, surface emissivities, and thresholds. The *Terra* orbit was selected to maximize clear-sky detection over land before land-surface heating causes the development of clouds and after early morning fog or stratus have dissipated. This fixed local-time sampling contrasts with the 24-h sampling by the TRMM VIRS. Thus, some of the differences are caused by discrepancies in the local time sampling of the two satellites.

The relative sampling differences between *Aqua* and *Terra* are a bit easier to understand since they are both polar orbiters with fixed overpass times. The mean July 2004 daytime *Aqua* and *Terra* cloud fractions and their differences are shown in Fig. 19. A cursory examination of the means (Fig. 19a, b) indicates that they are very similar. Dissimilarities stand out better in the difference plot (Fig. 19c) where light green and yellow indicate good agreement, blues show that *Terra* has more cloud cover, and reds and white correspond to greater *Aqua* cloud amounts. Increased afternoon cloudiness is greatest over elevated land areas, some coastal lands, and over the tropical western Pacific. Greater midmorning (*Terra*) cloud cover is apparent over the subtropical marine stratus regions, northwest of Australia, and over the northern Amazon Basin. While the cloud cover difference is relatively small over many areas, overall for this month, it appears that cloudiness is greater around 1330 LT than at 1030 LT.

Although the differences vary from month to month, the mean 2005 cloud amounts (Fig. 20) reveal some significant systematic zonal divergences. During the daytime (Fig. 20a), more

clouds are detected using the *Aqua* data over the Tropics and northern midlatitudes. Fewer clouds are seen over the southern midlatitudes. Relatively good agreement between *Terra* and *Aqua* is seen in the polar regions, except at night (Fig. 20b). In other zones, the nighttime cloud cover from *Aqua* tends to be the same or slightly less than that from *Terra*. When all hours are combined (Fig. 20c), the differences over non-polar ocean range between -0.03 and 0.02, with the largest differences occurring near the Equator and 40°S. Over land, *Aqua* systematically yields more clouds, by up to 6% at 12°S. The diurnal cycle in cloud cover over land is likely responsible for much of the *Aqua*-*Terra* bias. The large relative bias over the polar regions is primarily due to algorithm changes between *Terra* and *Aqua* [10]. Otherwise, in non-polar regions, the CERES *Terra* and *Aqua* results are generally very consistent given their sampling differences.

C. Comparisons with Other Cloud Amounts

Figure 21 shows the long-term zonal average cloud amounts from various sources including the ISCCP, MAST (MYD08 and MOD08), surface observations, and the three CERES datasets discussed here. Averages from those datasets are listed in Table 6. Although different in magnitude, the relative zonal variations are all very similar except north of 70°N and between 40°S and 70°S where the surface values are noisier, most likely as the result of sparse spatial sampling. In Tropics, the MYD08 amounts are the greatest and the CERES *Terra* amounts are the least. The CERES values are generally closest to the historical surface averages except in the Arctic and near 20°N. The ISCCP amounts fall between the surface and MAST results, except in the midlatitudes where they are the largest. Overall, the CERES cloud amounts differ from the from the MAST and ISCCP cloud amounts by 0.07 globally and between 60°N and 60°S. The

average difference between the surface and CERES cloud amounts is between 0.00 and 0.01 (Table 6).

Active sensors, including the Geoscience Laser Altimetry System (GLAS) on the Ice Cloud and Elevation Satellite and the Cloud-Aerosol Lidar and Infrared Pathfinder Satellite Observations (CALIPSO) satellite, detect even more cloud cover than any of the passive sensors. The CERES global cloud fractions are 0.00 to 0.08 less than those from GLAS [42] and 0.14 less those from CALIPSO [43]. Direct comparisons with an airborne lidar system [44] revealed that the CERES algorithm fails to detect most clouds with optical depths smaller than 0.3. Very preliminary estimates from CALIPSO measurements indicate that the cloud amounts having optical depths less than 0.3 is slightly more than 0.19 [Y. Hu, 2007, personal communication]. Nearly 70% of those thin clouds detected by CALIPSO have optical depths less than 0.1. Thus, it is likely that the primary difference between the CERES and the CALIPSO and GLAS cloud retrievals is due to the inability of the CERES algorithms to detect clouds that have very low effective optical depths. These would include such clouds as thin cirrus that fills the imager pixel or small cumulus clouds that partially fill the pixel. The surface-based cloud amounts may be similar in magnitude to the CERES values because surface observers may not see the very thin clouds or may discount their contribution to sky cover.

The large range in cloud cover derived from the same satellite data seen in Table 6, i.e., CERES and MAST, could be due to the sensitivity of the algorithms to cloud optical thickness. This probable cause may be reflected in the relative number of cloudy pixels having no retrievals of cloud properties. When determining cloud properties, it becomes difficult to obtain a valid retrieval for very low optical depths because the errors in the input parameters often exceed the size of the cloud signal. To avoid no retrievals, the ISCCP algorithm assigns to many of those

pixels a default minimum optical depth and a temperature that is 5 K less than the tropopause temperature [45]. In addition to having thin cloud no-retrievals, the MAST Collection-5 algorithm does not attempt to retrieve cloud properties for pixels on the edges of cloud decks where the retrieval may have a large uncertainty [46].

To examine the impact of no retrievals on the cloud fraction having cloud properties, the number of pixels identified as cloudy by the MAST scene identification algorithm [6] and the number of pixels having retrieved cloud properties [8] were computed using the Collection-5 MOD06 product for daytime during 30 July 2005 to determine the fraction of no-retrieval cloudy pixels. It was found that no-retrievals for the 3.7-μm retrieval--the MAST retrieval method having the greatest number of retrievals--comprise nearly 20% of the non-polar MAST *Terra* cloudy pixels compared to less than 4% of those from CERES. Assuming that the single day's statistics are typical, the cloud fractions for non-polar pixels having retrieved cloud properties are around 0.576 and 0.536 for CERES and MAST, respectively, whereas the ISCCP cloud fraction would be the same as that in Table 6 because of the default value approach. Presumably, the differences between CERES and the MAST retrieved cloud fractions are due to edge pixels and optically thin clouds not retrieved by the MAST algorithms. Since most of the clouds missed by CERES are very thin optically, they should have minimal impact on the radiation field. If they were detected, it appears that it would be very difficult to retrieve the corresponding cloud properties with much certainty. Nevertheless, to fully account for the impact of all clouds, it would be necessary to make such retrievals or to estimate their properties in some fashion, e.g., as in the ISCCP algorithm.

Other factors that affect cloud detectability include very high solar zenith angles (i.e., the twilight zone) and aerosols. When the aerosol optical depth is very large, as sometimes occurs

during dust storms, the CERES non-polar algorithm often misclassifies the heavy aerosol areas as cloudy. Because dust aerosols often produce multispectral radiance combinations that do not fit the model-computed radiances for clouds, some of those pixels end up as no retrievals while others have abnormal cloud properties, a topic discussed in [11]. The net impact of misclassified aerosols is a slight increase in cloud cover. In the twilight zone, the loss of the BTD_{34} signal for low clouds causes a slight net decrease in the cloud cover.

VI. Concluding Remarks

A multispectral algorithm has been developed for CERES to discriminate clouds from cloud-free scenes in non-polar regions primarily using channels common to both VIRS and MODIS to maintain some consistency across platforms. It has already been applied to many years of VIRS and MODIS data. Although it produces cloud amounts that are up to 10% less than those determined from other techniques and satellite data, the methodology appears to be quite successful at consistently detecting most clouds that are of radiative significance and correspond to those seen from the surface. Further validation and error assessment studies are needed to fully quantify the impact of any undetected clouds.

Through cross-calibration, it was found that several of the channels common to VIRS, *Terra* MODIS, and *Aqua* MODIS are inconsistent. The VIS channel calibration differences have been discussed elsewhere [16]. The radiances measured by the 1.6-μm channel on the VIRS are too low by 19% compared to the corresponding *Terra* MODIS channel. The *Terra* 3.8-μm channel also shows some significant differences compared with the same channel on *Aqua*. It is important that users of the MODIS data recognize these discrepancies. Future editions of the CERES algorithms will take them into account during processing.

Given that CERES was short-lived on TRMM and the 1.6-μm channel failed on *Aqua* MODIS, the cross-platform consistency requirement between the VIRS and MODIS masks is no longer critical except between *Aqua* and *Terra* MODIS. Thus, in the future, additional channels from the MODIS, such as the CO_2-absorption channels and the high resolution VIS channel could be used to improve the detection of small cumulus and thin cirrus that are currently missed using the software editions described here. Other channels could also be used to improve separation of aerosols and clouds.

Because it relies on channels that are used on many operational meteorological satellites, the current CERES non-polar mask has already been adapted for use with several of those satellites, e.g., [47]. Combined with the CERES polar mask [10] and cloud property retrieval [11] algorithms and the CERES scanner radiances, it has produced numerous valuable data products covering much of the past decade. Those products have already advanced our understanding of the radiative impact of clouds, e.g., [2, 48] and their interaction with the climate system, e.g., [49, 50]. They have the potential for many other uses in the future.

ACKNOWLEDGMENT

This research has been supported by the NASA Science Mission Directorate through the CERES Project. Thanks to Norman Loeb and other members of the CERES Science Team who have made constructive comments and suggestions that contributed to the development of these algorithms. The satellite data were processed at the NASA Langley Research Center Distributed Active Archive Center.

REFERENCES

[1] Wielicki, B. A., et al., "Clouds and the Earth's Radiant Energy System (CERES): Algorithm overview," IEEE Trans. Geosci. Remote Sens., vol. 36, pp. 1127-1141, 1998.

[2] Loeb, N. G., N. Manalo-Smith, S. Kato, W. F. Miller, S. Gupta, P. Minnis, and B. A. Wielicki, "Angular distribution models for top-of-atmosphere radiative flux estimation from the Clouds and the Earth's Radiant Energy System instrument on the Tropical Rainfall Measuring Mission satellite. Part I: Methodology," J. Appl. Meteorol., vol. 42, pp. 240-265, 2003.

[3] Wielicki, B. A., R. D. Cess, M. D. King, D. A. Randall, and E. F. Harrison, "Mission to planet Earth: Role of clouds and radiation in climate," Bull. Amer. Meteorol. Soc., vol. 76, pp.2125-2153, 1995.

[4] Wielicki, B. A., B. R. Barkstrom, E. F. Harrison, R. B. Lee, III, G. L. Smith, and J. E. Cooper, "Clouds and the Earth's Radiant Energy System (CERES): An Earth Observing System experiment," Bull. Amer. Meteorol. Soc., vol. 77, pp. 853-867, 1996.

[5] Rossow, W. B. and R. A. Schiffer, "Advances in understanding clouds from ISCCP," Bull Am. Meteor. Soc., vol. 80, pp. 2261-2287, 1999.

[6] Ackerman, S. A., K. I. Strabal, W. P. Menzel, R. A. Frey, C. C. Mueller, and L. E. Gumley, "Discriminating clear sky from clouds with MODIS," J. Geophys. Res., vol. 103, pp. 32 141–32 157, 1998

[7] King, M. D., et al., "Cloud and aerosol properties , precipitable, water, and profiles of temperature and water vapor," IEEE Trans. Geosci. Remote Sens., vol. 41, pp. 442-458.

[8] Platnick, S., M. D. King, S. A. Ackerman, W. P. Menzel, B. A. Baum, J. C. Riedl, and R. A. Frey, "The MODIS cloud products: Algorithms and examples from Terra," IEEE Trans. Geosci. Remote Sens., vol. 41, 459-473.

[9] Young, D. F., P. Minnis, G. G. Gibson, D. R. Doelling, and T. Wong, "Temporal interpolation methods for the clouds and Earth's Radiant Energy System (CERES) Experiment," J. Appl. Meteorol., vol. 37, pp. 572-590, 1998.

[10] Trepte, Q. Z, P. Minnis, D. A. Spangenberg, R. F. Arduini, S. Sun-Mack, and Y. Chen, "Polar cloud and snow discrimination for CERES using MODIS data," IEEE Trans. Geosci. Remote Sens., in preparation fof submission, 2008. [For immediate reference, use: Trepte, Q., P. Minnis, and R. F. Arduini, "Daytime and nighttime polar cloud and snow identification using MODIS data," Proc. SPIE 3rd Intl. Asia-Pacific Environ. Remote Sensing Symp., Hangzhou, China, October 23-27, vol. 4891, 449-459, 2002.]

[11] Minnis, P., S. Sun-Mack, D. F. Young, P. W. Heck, D. P. Garber, Y. Chen, D. A. Spangenberg, B. A. Wielicki, and E. B. Geier, "Cloud property retrievals for CERES using TRMM VIRS and Terra and Aqua MODIS data," IEEE Trans. Geosci. Remote Sens., in preparation for submission, 2008. [For immediate reference, use: Minnis, P., et al., "Cloud Optical Property Retrieval (Subsystem 4.3). "Clouds and the Earth's Radiant Energy System (CERES) Algorithm Theoretical Basis Document, Volume III: Cloud Analyses and Radiance Inversions (Subsystem 4)," NASA RP 1376 Vol. 3, edited by CERES Science Team, pp. 135-176, 1995.]

[12] Sun-Mack, P. Minnis, Y. Chen, R. F. Arduini, and D. F. Young, "Visible clear-sky and near-infrared surface albedos derived from VIRS and MODIS data for CERES," IEEE Trans. Geosci. Remote Sens., in preparation for submission, 2008. [For immediate reference, use: Chen, Y., S. Sun-Mack, P. Minnis, and R. F. Arduini, "Clear-sky narrowband albedo variations derived from VIRS and MODIS data," Proc. AMS 12th Conf. Atmos. Radiation, Madison, WI, July 10-14, CD-ROM, 5.6, 2006.]

[13] Kummerow, C. W. Barnes, T. Kozu, J. Shine, and J. Simpson, "The Tropical Rainfall Measuring Mission System (TRMM) sensor package," J. Atmos. Oceanic Technol., vol. 15, pp. 809-827, 1998.

[14] Minnis, P., L. Nguyen, D. R. Doelling, D. F. Young, W. F. Miller, and D. P. Kratz, "Rapid calibration of operational and research meteorological satellite imagers, Part I: Evaluation of research satellite visible channels as references," J. Atmos. Oceanic Technol., vol. 19, pp. 1233-1249, 2002.

[15] Minnis, P., L. Nguyen, D. R. Doelling, D. F. Young, W. F. Miller, and D. P. Kratz, "Rapid calibration of operational and research meteorological satellite imagers, Part II: Comparison of infrared channels," J. Atmos. Oceanic Technol., vol. 19, pp. 1250-1266, 2002.

[16] Minnis, P., D. R. Doelling, L. Nguyen, W. F. Miller, and V. Chakrapani, "Assessment of the visible channel calibrations of the TRMM VIRS and MODIS on *Aqua* and *Terra*," J. Atmos. Oceanic Technol., in press, 2007.

[17] Ignatov, A., "Spurious signals in TRMM/VIRS reflectance channels and their effect on aerosol retrievals," J. Atmos. Oceanic Technol., vol. 20, pp. 1120-1137, 2003.

[18] Ignatov, A., and L. L. Stowe, "Physical basis, premises, and self-consistency checks of aerosol retrievals from TRMM VIRS," J. Appl. Meteorol., vol. 39, pp. 2259-2277, 2000.

[19] Lyu, C. H., R. A. Barnes, and W. L. Barnes, "First results from on-orbit calibrations of the Visible and Infrared Scanner for the Tropical Rainfall Measuring Mission," J. Atmos. Oceanic Technol., vol. 17, pp.-385-394, 2000.

[20] Lyu, C.-H., and W. L. Barnes, "Four years of TRMM/VIRS on-orbit calibrations and characterization using lunar models and data from Terra/MODIS," J. Atmos. Oceanic Technol., vol. 20, pp. 333-347, 2003.

[21] Young, D. F., P. Minnis, and R. F. Arduini, "A comparison of cloud microphysical properties derived using VIRS 3.7 and 1.6 μm data," Proc. AMS 10th Conf. Atmos. Rad., Madison, WI, June 28–July 2, pp. 25-28, 1999.

[22] Barnes, W. L., T. S. Pagano, and V. V. Slomonson, "Prelaunch characteristics of the Moderate Resoluiton Imaging Spectroradiometer (MODIS) on EOS-AM1," IEEE Trans. Geosci. Remote Sens., vol. 36, pp. 1088-1100.

[23] Yang, S.-K., S. Zhou, and A. J. Miller, "SMOBA: A 3-dimensional daily ozone analysis using SBUV/2 and TOVS measurements." (http://www.cpc.ncep.noaa.gov/products/stratosphere/SMOBA/smoba_doc.shtml)

[24] Bloom, S., A. da Silva, D. Dee, M. Bosilovich, J.-D. Chern, S. Pawson, S. Schubert, M. Sienkiewicz, I. Stajner, W.-W. Tan, M.-L. Wu, "Documentation and Validation of the Goddard Earth Observing System (GEOS) Data Assimilation System - Version 4 ," Technical Report Series on Global Modeling and Data Assimilation 104606, 26, 2005.

[25] Gupta, S. K., N. A. Ritchey, F. G. Rose, T. L. Alberta, T. P. Charlock, and L. H. Coleman, "Regrid humidity and temperature fields (system 12.0). CERES Algorithm Theoretical Basis Document Release 2.2," NASA RP 1376, 20 pp., 1997. http://asd-www.larc.nasa.gov/ATBD/ATBD.html]

[26] Nolin, A., R.L. Armstrong, and J. Maslanik, "Near Real-Time SSM/I EASE-Grid Daily Global Ice Concentration and Snow Extent, January to March 2004," National Snow and Ice Data Center, 1998, updated daily. http://nsidc.org/data/docs/daac/nise1_nise.gd.html.

[27] Ramsay, B. H., "The interactive multisensor snow and ice mapping system," Hydrol. Processs., vol. 12, pp. 1537-1546, 1998.

[28] Sun-Mack, S., Y. Chen, T. D. Murray, P. Minnis, and D. F. Young, "Visible clear-sky and near-infrared surface albedos derived from VIRS for CERES" Proc. AMS 10th Conf. Atmos. Rad., Madison, WI, June 28 – July 2, pp. 422-425, 1999.

[29] Belward, A. S., J. E. Estes, and K. D. Kline, "The IGBP-DIS 1-Km Land-Cover Data Set DISCover: A Project Overview," Photogrammetric Engr. and Remote Sens., vol. 65, p. 1013-1020, 1999.

[30] Minnis, P. and E. F. Harrison, "Diurnal variability of regional cloud and clear-sky radiative parameters derived from GOES data, Part I: Analysis method," J. Clim. Appl. Meteorol., vol. 23, pp. 993-1011, 1984.

[31] Suttles, J. T., R. N. Green, P. Minnis, G. L. Smith, W. F. Staylor, B. A. Wielicki, I. Walker, D. F. Young, V. R. Taylor, and L. L. Stowe, "Angular radiation models for Earth-atmosphere system, Vol. 1, Shortwave radiation," NASA RP-1184, 144 pp., 1988.

[32] Kriebel, K. T., "Measured spectral bidirectional reflectance properties of vegetated surfaces," Appl. Opt., vol. 17, pp. 253-259, 1978.

[33] Chen, Y., S. Sun-Mack, P. Minnis, D. F. Young, and W. L. Smith, Jr., "Surface emissivity derived for infrared remote sensing from satellites," Proc. AMS 11th Conf. Satellite Meteorology and Oceanography, Madison, WI, Oct. 15-18, 512-515, 2001.

[34] Chen, Y., S. Sun-Mack, P. Minnis, D. F. Young, and W. L. Smith, Jr., "Seasonal surface spectral emissivity derived from Terra MODIS data," Proc. 13th AMS Conf. Satellite Oceanogr. and Meteorol., Norfolk, VA, Sept. 20-24, CD-ROM, P2.4, 2004.

[35] Kratz, D. P., "The correlated *k*-distribution technique as applied to the AVHRR channels," J. Quant. Spectrosc. Radiat. Transfer, vol. 53, 501-517, 1995.

[36] Rose, F., T. P. Charlock, D. A. Rutan, and G. L. Smith, "Tests of a constraint algorithm for the surface and atmospheric radiation budget," Proc. AMS 9th Conf. Atmos. Rad., Long Beach, CA, 2-7 February, pp. 466-469, 1997.

[37] Baum, B. A, R. M. Welch, P. Minnis, L. L. Stowe, J. A. Coakley, Jr., J. Titlow, V. Tovinkere, P. W. Heck, Q. Trepte, D. R. Doelling, S. Mayor, T. Berendes, Q. Han, S. A. Christopher, K.-S. Kuo, M. Penaloza, A. Logar, and P. Davis, "Imager Clear-Sky Determination and Cloud Detection (Subsystem 4.1). Clouds and the Earth's Radiant Energy System (CERES) Algorithm Theoretical Basis Document, Volume III: Cloud Analyses and Radiance Inversions (Subsystem 4)," NASA RP 1376, vol. 3, pp. 43-82, 1995.

[38] Welch, R. M., S. K. Sengupta, A. K. Goroch, R. Palikonda, N. Rangaraj, and M. S. Navar, "Polar cloud and surface classification using AVHRR imagery-An intercomparison of methods", J. Appl. Meteorol., vol. 31, pp. 405-420, 1992.

[39] Minnis, P., D. P. Garber, D. F. Young, R. F. Arduini, and Y. Takano, "Parameterization of reflectance and effective emittance for satellite remote sensing of cloud properties," J. Atmos. Sci., vol. 55, 3313-3339, 1998.

[40] Saunders, R. W. and K. T. Kriebel, "An improved method for detecting clear sky and cloudy radiances from AVHRR data," Int. J. Remote Sens., vol. 9, pp. 123-150, 1988.

[41] Hahn, C. J., and S. G. Warren, "Extended edited synoptic cloud reports from ships and land stations over the globe, 1952–1996," NDP026C, Carbon Dioxide Information Analysis Center, Oak Ridge National Laboratory, Oak Ridge, TN, 80 pp., 1999.

[42] Minnis, P., S. Sun-Mack, Y. Chen, Q. Z. Trepte, and Y. Yi, "Comparison of CERES-MODIS and IceSat GLAS cloud amounts," Geophys. Res. Lett., submitted, 2008.

[43] Sun-Mack, S., B. A. Wielicki, P. Minnis, S. Gibson, and Y. Chen, "Integrated cloud-aerosol-radiation product using CERES, MODIS, CALISPO, and CloudSat data," Proc. SPIE Europe 2007 Conf. Remote Sens. Clouds and the Atmos.," Florence, Italy, 17-19 September, vol. 6745, no. 29, 2007.

[44] Chiriaco, M., H. Chepfer, P. Minnis, M. Haeffelin, S. Platnick, D. Baumgardner, P. Dubuisson, M. McGill, V. Noel, J. Pelon, D. Spangenberg, S. Sun-Mack, and G. Wind, "Comparison of CALIPSO-like, LaRC, and MODIS retrievals of ice cloud properties over SIRTA in France and Florida during CRYSTAL-FACE," J. Appl. Meteorol. Climatol, vol. 46, pp. 249-272, 2007.

[45] Rossow, W.B., A.W. Walker, D.E. Beuschel, and M.D. Roiter, "International Satellite Cloud Climatology Project (ISCCP) Documentation of New Cloud Datasets," WMO/TD-No. 737, World Meteorological Organization, 115 pp., 1996.

[46] Platnick, S. and M. D. King, "Update on the MODIS Collection 5 processing cloud optical depth and microphysical algorithm and product validation," Proc. OSA 2007 FTS/HISE Topical Mtg.and Tabletop Exhibit, 12-15 Feb., CD-ROM, HTuA1, 2007.

[47] Minnis, P., W. L. Smith, Jr., L. Nguyen, D. A. Spangenberg, P. W. Heck, R. Palikonda, J. K. Ayers, C. Wolff, and J. J. Murray, "Near-real time cloud properties and aircraft icing indices from GEO and LEO satellites," Proc. SPIE 49th Ann. Mtg., Weather and Environ. Satellties Conf., Denver, CO, August 2-3, vol. 5549, pp. 145-155, 2004.

[48] Wielicki, B. A., T. M. Wong, R. P. Allan, A. Slingo, J. T. Kiehl, B. J. Soden, B. J., C. T. Gordon, A. J. Miller, S. K. Yang, D. A. Randall, F. Robertson, J. Susskind, and H. Jacobowitz, "Evidence for large decadal variability in the tropical mean radiative energy budget," Science, vol. 295, pp. 841-844, 2002.

[49] Wielicki, B. A., T. Wong, N. Loeb, P. Minnis, K. Priestley, and R. Kandel,"Changes in Earth's albedo measured by satellites," Science, 308, p. 825, 2005.

[50] Kato, S., N. G. Loeb, P. Minnis, J. A. Francis, T. P. Charlock, D. Rutan, E. E. Clouthiaux, and S. Sun-Mack, "Seasonal and interannual variations of top-of-atmosphere irradiance and cloud cover over polar regions derived from the CERES data set," Geophys. Res. Lett., vol. 33, L19804, 10.1029/2006GL026685, 2005.

Table Captions

Table 1. Imager channels ingested in CERES processing and used in CERES cloud mask. VIRS data are 2-km resolution. All MODIS data are 1-km resolution, except for channel 1, which has both 1 and 0.25 km resolutions.

Table 2. Average differences in matched brightness temperatures from thermal channel intercalibrations.

Table 3. Constraint values for reflectance ratio tests.

Table 4. Summary of daytime cloud mask tests used to reach final classification of all non-polar pixels for *Terra* MODIS, March 2000.

Table 5. Summary of nighttime cloud mask tests used to reach final classification of all non-polar pixels for *Terra* MODIS, March 2000.

Table 6. Mean cloud amounts from long-term measurements.

Figure Captions

Fig. 1. Intercalibration of VIRS channel-2 and *Terra* MODIS channel-6 radiances over ocean for (a) March and (b) September 2001.

Fig. 2. Intercalibration of *Aqua* and *Terra* MODIS channel-20 brightness temperatures during August 2004 during the (a) day and (b) night.

Fig. 3. CERES *Terra* MODIS clear radiation parameters for January 2001 mean (a) VIS clear-sky overhead sun albedo, (b) 1.62-μm overhead-sun surface albedo, (c) 3.79-μm and (d) 10.8-μm surface emissivities.

Fig. 4. Schematic diagram of CERES cloud processing system. Unshaded areas correspond to the scene identification process.

Fig. 5. Outline of daytime scene identification process. Shading indicates use in *Aqua* Ed1a only.

Fig. 6. Final classification for certain pixels classified as (a) clear or (b) cloudy after all of the B tests. If the specified conditions are met, the pixel is reclassified. SGP refers to sunglint probability.

Fig. 7. Thin cirrus tests used for *Aqua* Ed 1a processing after **B** Tests are applied.

Fig. 8a. Daytime, **C1** test over land. $B1 = 0$, $B2 = 1$, $B3 = 1$. The relaxation factor, f_r, is 2.0 for desert and 1.5 for non-desert land. Parameters shown in italics indicate tests only used by *Aqua* Ed1. The T_{skin} test for b=1, c=1 is only used for *Terra* Ed2. The free-floating tests are applied only to certain surface types after the **C1** tests are completed.

Fig. 8b. Same as Fig. 8a, except over ocean.

Fig. 9. Ocean sunglint tests. Italics denote tests only used for *Aqua* Ed1.

Fig. 10. *Terra* MODIS image and VIS reflectance and mask input and clear-sky VIS parameters, 1700 UTC, 21 December 2000. (a) RGB image, (b) water percentage map, (c) snow-ice map, (d) overhead-sun clear-sky albedo, (e) normalized directional reflectance, (f) clear-sky albedo, (g) BRDF factor, (h) predicted clear-sky reflectance, (i) observed reflectance.

Fig. 11. *Terra* MODIS image, IR temperature, and BTD and mask input and predicted clear-sky IR and BTD parameters, 1700 UTC, 21 December 2000. (a) RGB image, (b) MOA skin temperature, (c) MOA precipitable water vapor in cm, (d) IR surface emissivity, (e) predicted clear-sky IR brightness temperature T_{cs4}, (f) observed IR brightness temperature, (g) 3.8-μm surface emissivity, (h) predicted clear-sky BTD_{cs34}, (i) observed BTD_{34}.

Fig. 12. Pixel classification by CERES daytime non-polar cloud mask for *Terra* MODIS image in Fig. 11a, 1700 UTC, 21 December 2000. (a) final tests used to classify each pixel, (b) cloud quality classification, (c) final cloud mask, (d) final clear-sky classifications.

Fig. 13. Schematic diagram of CERES non-polar nighttime scene identification.

Fig. 14. Flow diagram for twilight tests applied when nighttime mask identifies pixels as good clear and significant sunlight affects the SIR brightness temperature.

Fig. 15. Nighttime **E1** test applied when *D1* =1, *D2* = 1, and *D3* = 0.

Fig. 16. CERES nocturnal cloud mask for VIRS data taken at 6 UTC, 25 March 2001 over Texas.

Fig. 17a. Mean CERES daytime cloud amount for March 2000 from (top) *Terra* MODIS and (bottom) TRMM VIRS.

Fig. 17b. Same as Fig. 17a, except for nighttime.

Fig. 18. Mean zonal cloud fraction and differences for summer 2000 (JJA) and winter 2001 (DJF).

Fig. 19. Mean cloud fraction distributions and differences for July 2004.

Fig. 20. Mean 2005 CERES zonal cloud fraction and difference.

Fig. 21. Mean long-term zonal cloud amounts from several sources. The time periods and averages are listed in Table 6.

Table 1. Imager channels ingested in CERES processing and used in CERES cloud mask. VIRS data are 2-km resolution. All MODIS data are 1-km resolution, except for channel 1, which has both 1 and 0.25 km resolutions.

CERES Reference Channel #	VIRS Channel #	Central Wavelength (μm)	MODIS Channel #	Central Wavelength (μm)	Use
1	1	0.620	1	0.645	All
2	2	1.610	6	1.640	1,2,3
3	3	3.780	20	3.792	All
4	4	10.83	31	11.030	All
5	5	12.01	32	12.020	All
6			29	8.550	2,3,4,5
7			7	2.130	4,5
8			26	1.375	4
9			27	6.720	3,5
10			2	0.858	
11			3	0.469	
12			4	0.555	
13			5	1.240	
14			17	0.905	
15			23	4.050	
16			33	13.34	
17			34	13.64	
18			35	13.94	
19			36	14.24	

Use Key:
1 - VIRS Edition 2
2 – *Terra* Edition 2 Nonpolar
3 - *Terra* Edition 2 Polar
4 - *Aqua* Edition 1 Nonpolar
5 - *Aqua* Edition 1 Polar

Table 2. Average differences in matched brightness temperatures from thermal channel intercalibrations.

Satellite Pair	3.8 μm (K)		10.8 μm (K)		12.0 μm (K)	
	Day	Night	Day	Night	Day	Night
VIRS-*Aqua*	-0.85	-0.35	0.26	-0.08	-0.94	-0.83
VIRS-*Terra*	-1.39	-1.01	0.21	-0.06	-1.00	-0.88
Terra - *Aqua*	0.55	2.29	0.01	0.16	0.04	0.16

Table 3. Constraint values for reflectance ratio tests.

Parameter	Conditions	Formula
r_{23g}	sunglint	$r_{23g} = 0.005$ SGP + 1
r_{21c}	sun glint ocean	$r_{21c} = 0.18\ \mu + 0.625$
r_{21c}	non-glint ocean	$r_{21c} = 0.20\ \mu + 0.587$
r_{21c}	desert	$r_{21c} = 0.843$
r_{21c}	non-desert land	$r_{21c} = 0.572$
r_{21c}	Non-polar snow	$r_{21c} = 044$

Table 4. Summary of daytime cloud mask tests used to reach final classification of all non-polar pixels for *Terra* MODIS, March 2000.

Test		Ocean	Land	Desert	Total
A:	T_{lim} Cloud	0.481	0.309	0.077	0.431
All B:	Clear	0.161	0.250	0.764	0.195
All B:	Cloud	0.209	0.189	0.028	0.201
C1:	BTD_{34}, VIS	0.043	0.055	0.010	0.046
C2:	BTD_{34}	0.037	0.046	0.017	0.039
C3:	VIS	0.025	0.065	0.065	0.035
C4:	IR, BTD_{34}	0.013	0.022	0.020	0.015
C5:	IR	0.015	0.018	0.011	0.016
C6:	IR, VIS	0.013	0.030	0.005	0.017
	Bad Data	0.004	0.011	0.002	0.006

Table 5. Summary of nighttime cloud mask tests used to reach final classification of all non-polar pixels for *Terra* MODIS, March 2000.

Test	Ocean	Land	Desert	Total
A: T_{lim} Cloud	0.483	0.353	0.082	0.447
All D: Clear	0.208	0.343	0.684	0.245
E1: IR, BTD_{34} high	0.077	0.111	0.073	0.084
E2: BTD_{34} low	0.003	0.034	0.058	0.010
E3: BTD_{34} high	0.005	0.043	0.052	0.014
E4: IR, BTD_{34} low	0.067	0.036	0.006	0.060
E5: IR	0.161	0.072	0.022	0.141
Bad Data	0.000	0.000	0.000	0.000

Table 6. Mean cloud amounts from long-term measurements.

Source	Time Period	Global		37.5°S – 37.5°N
Surface	1971-1996	0.601	0.590	0.554
ISCCP	1983-2001	0.675	0.673	0.621
MOD08 *Terra*	2000-2005	0.668	0.662	0.614
MYD08 *Aqua*	2002-2005	0.678	0.677	0.632
CERES *Terra*	2000-2005	0.602	0.597	0.543
CERES *Aqua*	2002-2005	0.604	0.595	0.543
CERES VIRS	1998-2000	N/A	N/A	0.554

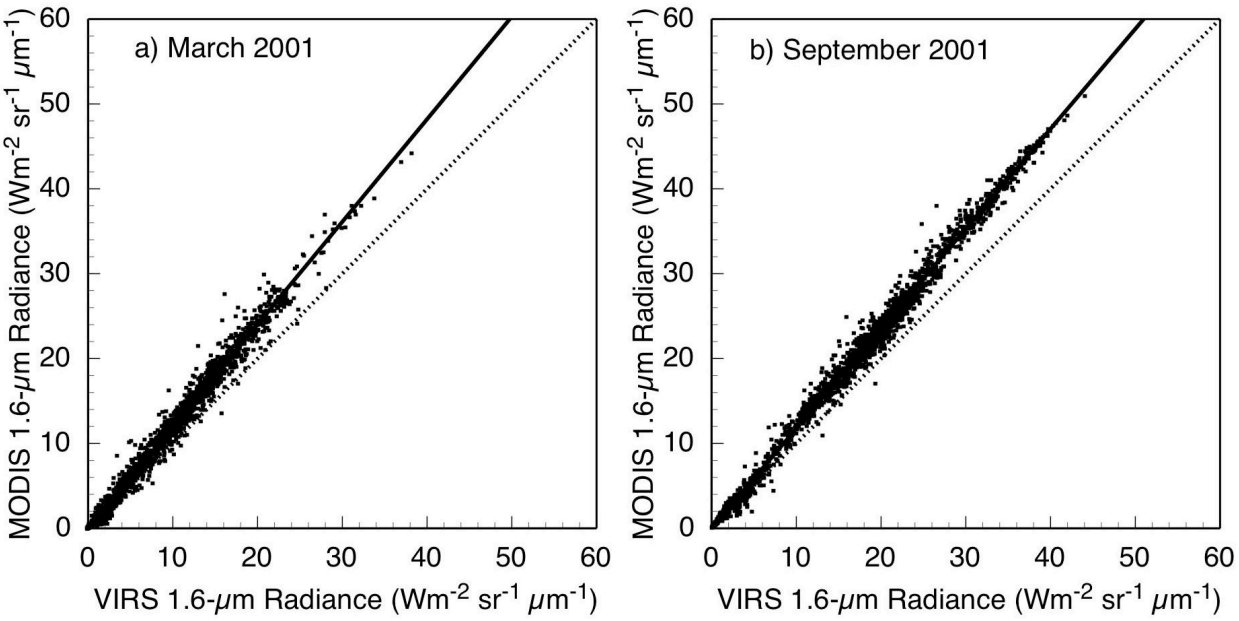

Fig. 1. Intercalibration of VIRS channel-2 and *Terra* MODIS channel-6 radiances over ocean for (a) March and (b) September 2001.

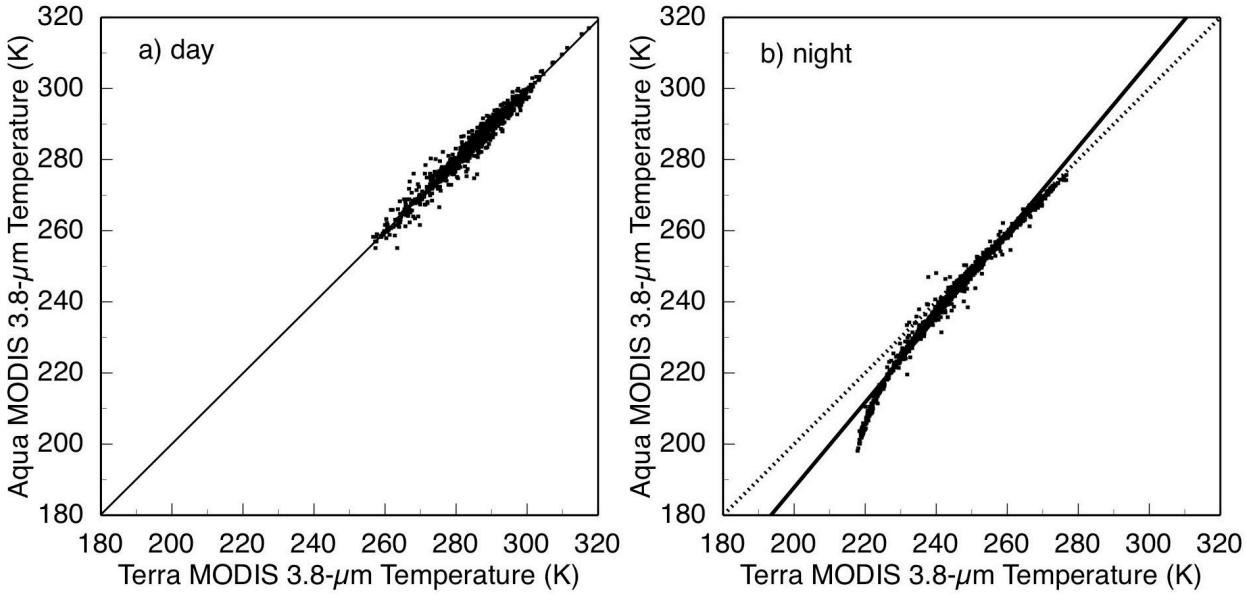

Fig. 2. Intercalibration of *Aqua* and *Terra* MODIS channel-20 brightness temperatures during August 2004 during the (a) day and (b) night.

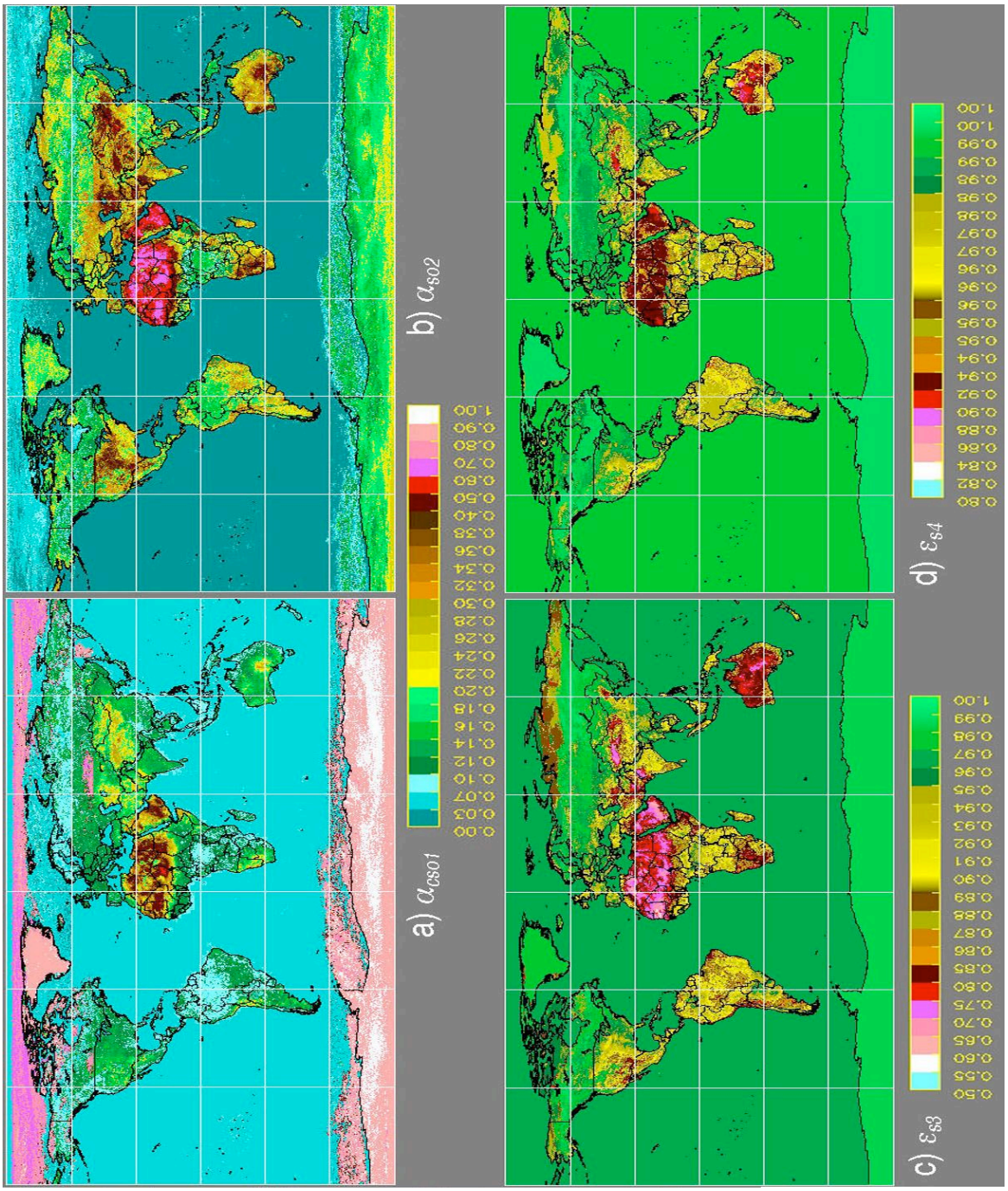

Fig. 3. CERES *Terra* MODIS clear radiation parameters for January 2001 mean (a) VIS clear-sky overhead sun albedo, (b) 1.62-µm overhead-sun surface albedo, (c) 3.79-µm and (d) 10.8-µm surface emissivities.

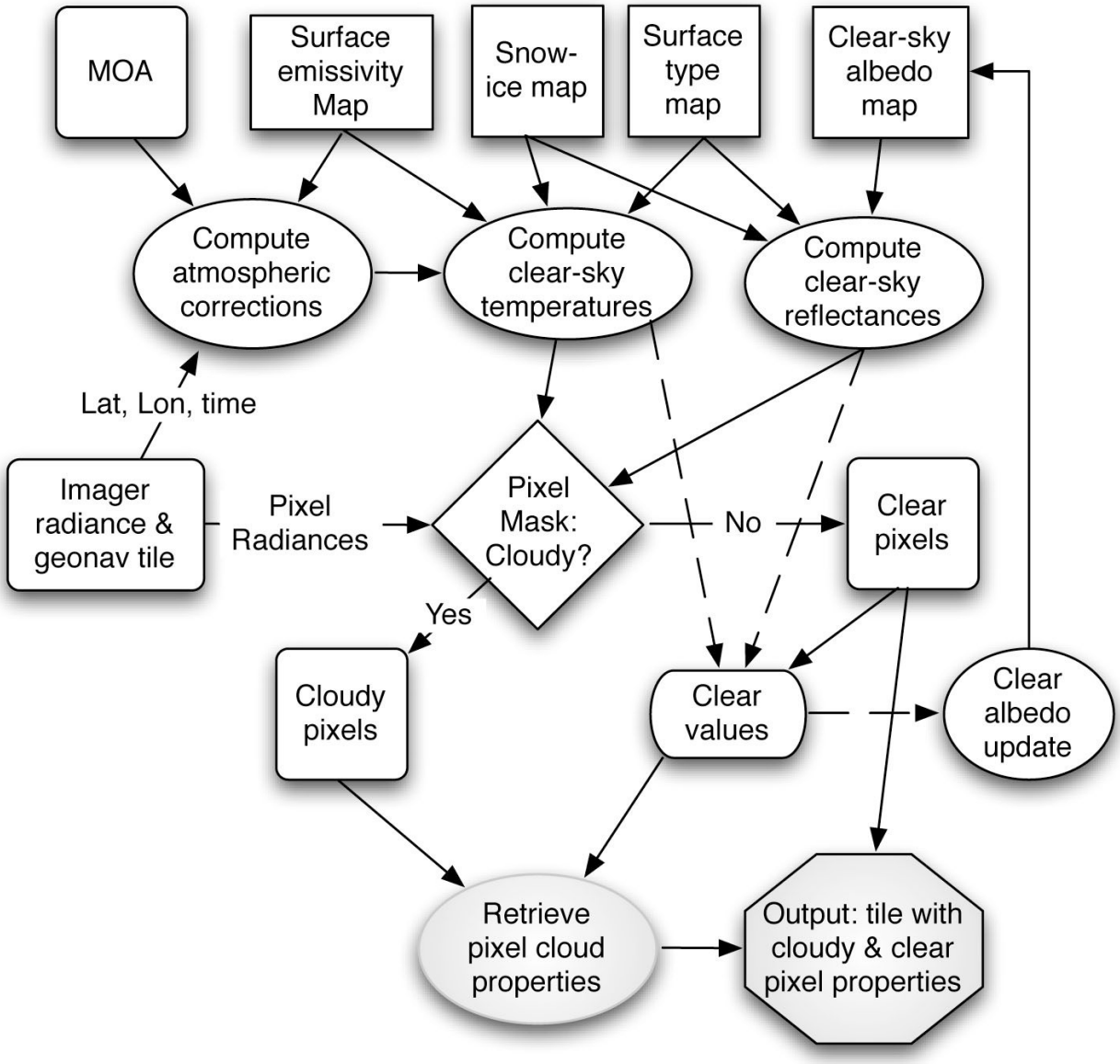

Fig. 4. Schematic diagram of CERES cloud processing system. Unshaded areas correspond to the scene identification process.

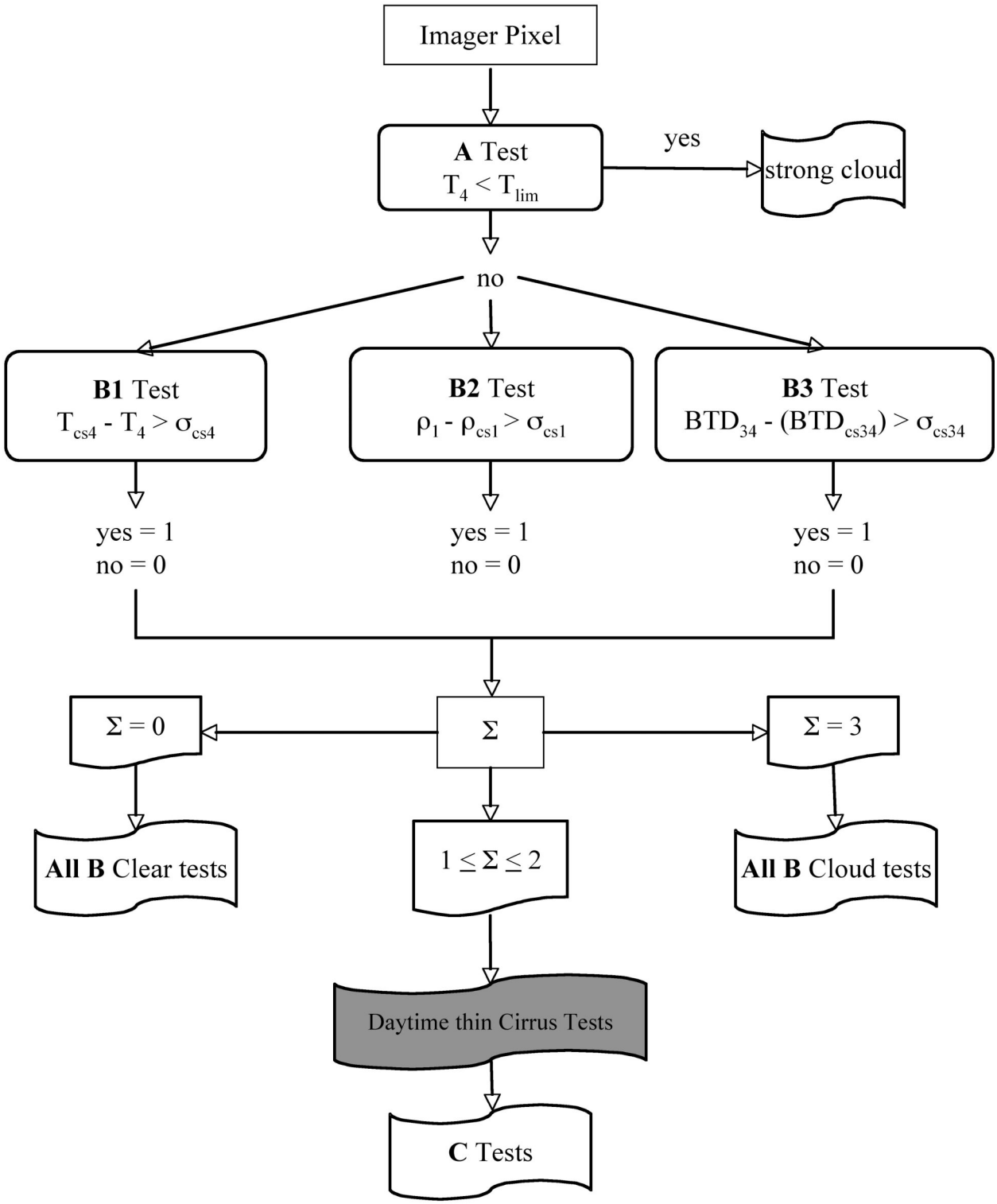

Fig. 5. Outline of daytime scene identification process. Shading indicates use in *Aqua* Ed1a only.

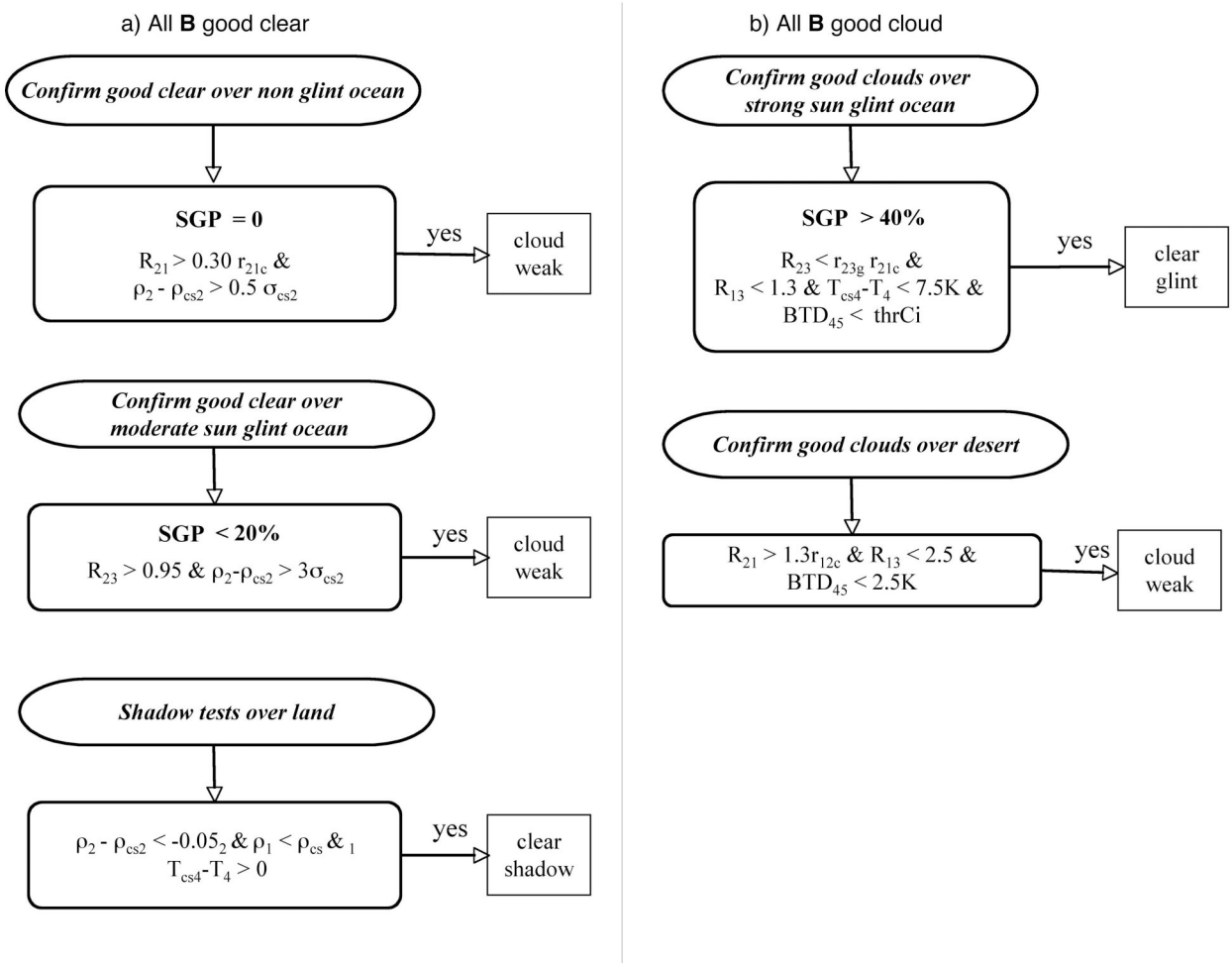

Fig. 6. Final classification for certain pixels classified as (a) clear or (b) cloudy after all of the B tests. If the specified conditions are met, the pixel is reclassified. SGP refers to sunglint probability.

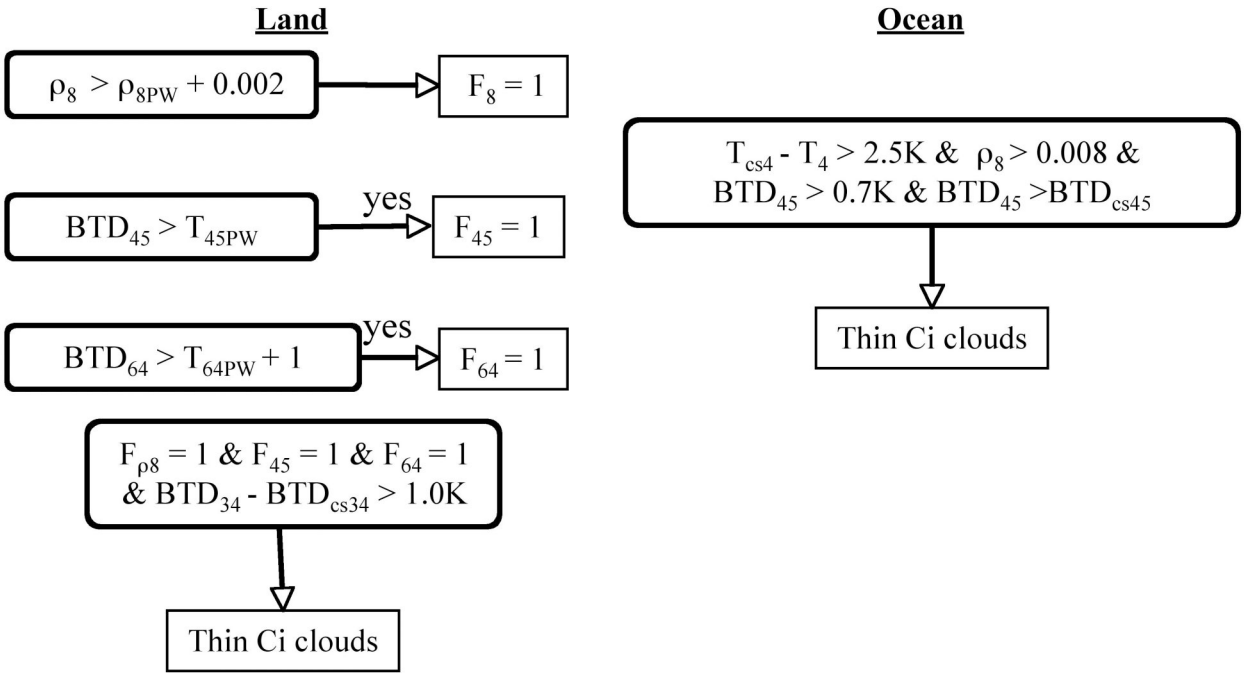

Fig. 7. Thin cirrus tests used for *Aqua* Ed 1a processing after **B** Tests are applied.

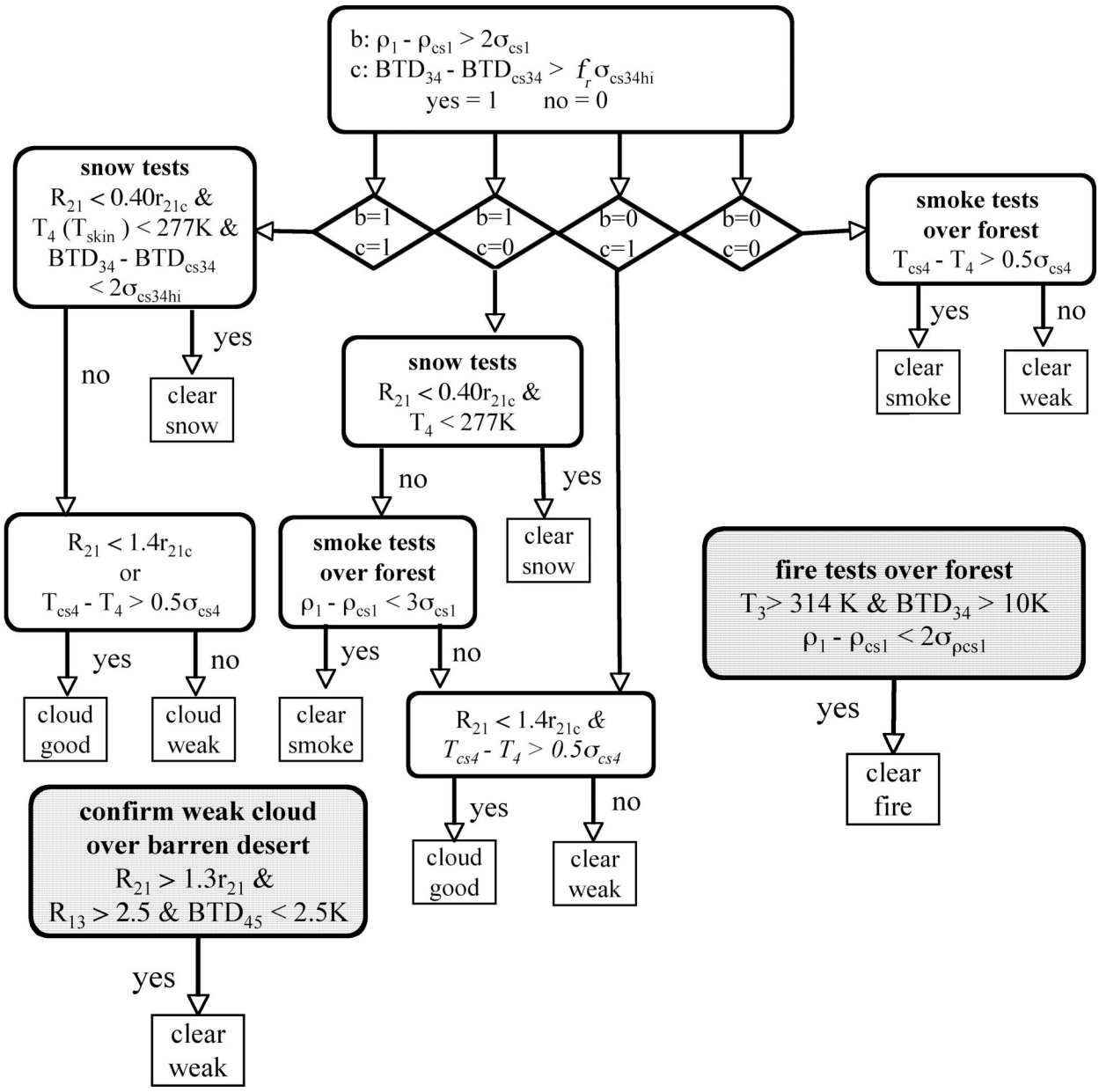

Fig. 8a. Daytime, **C1** test over land. *B1* = 0, *B2* = 1, *B3* = 1. The relaxation factor, f_r, is 2.0 for desert and 1.5 for non-desert land. Parameters shown in italics indicate tests only used by *Aqua* Ed1. The T_{skin} test for b=1, c=1 is only used for *Terra* Ed2. The free-floating tests are applied only to certain surface types after the **C1** tests are completed.

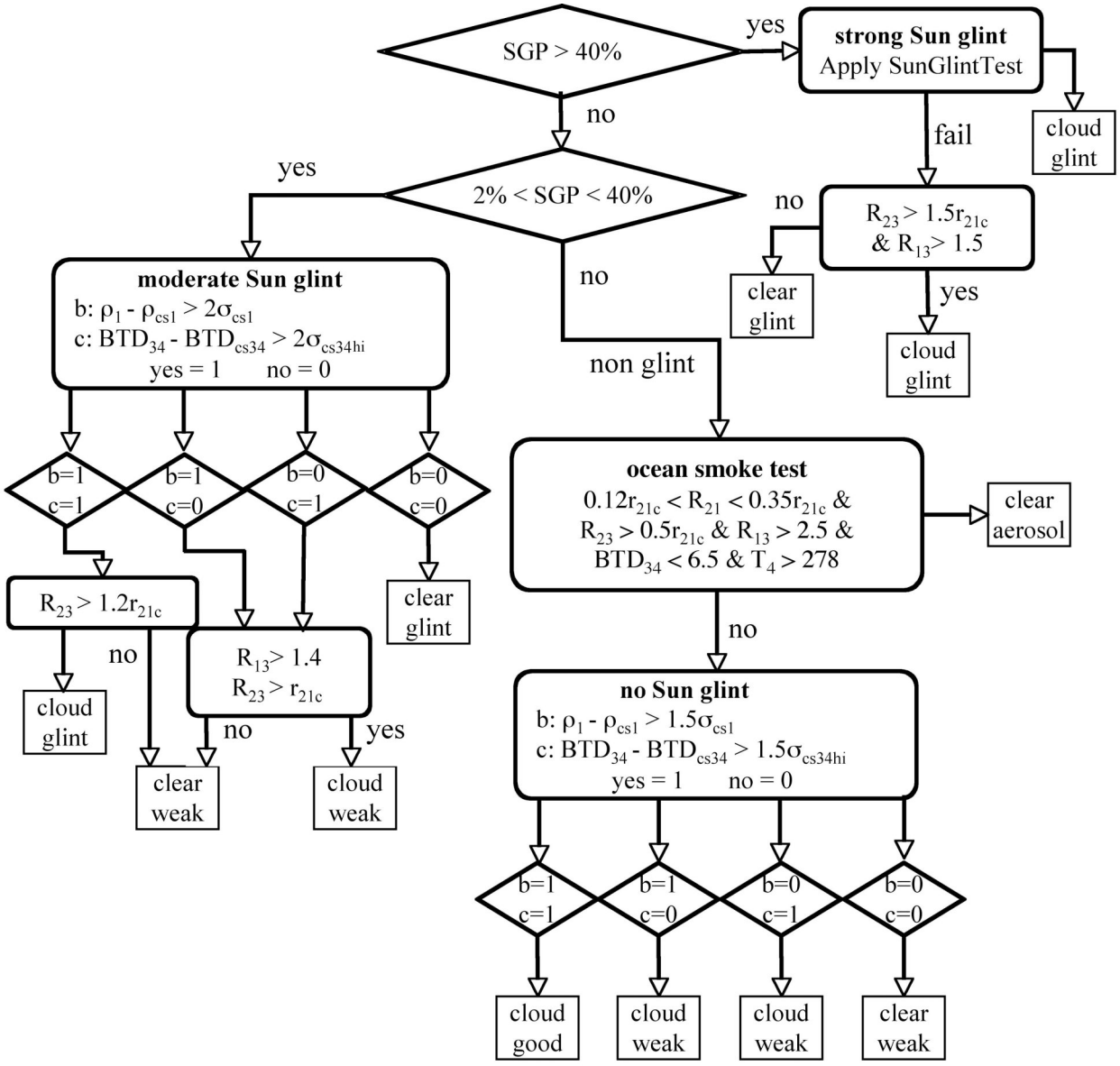

Fig. 8b. Same as Fig. 8a, except over ocean.

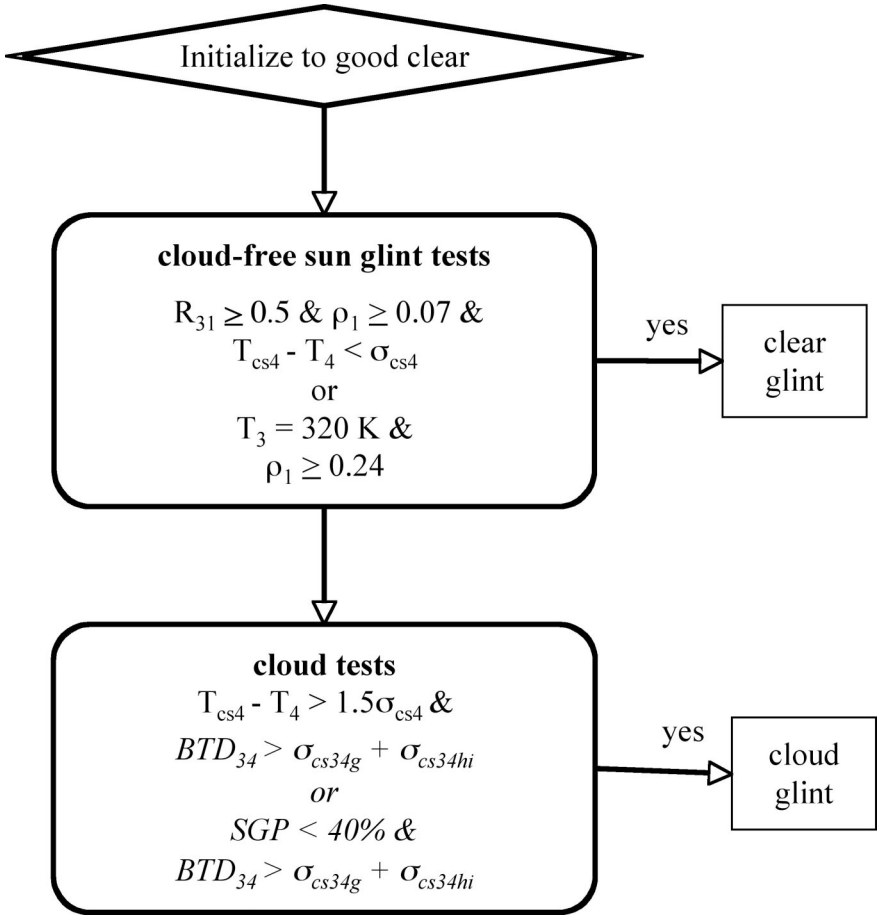

Fig. 9. Ocean sunglint tests. Italics denote tests only used for *Aqua* Ed1.

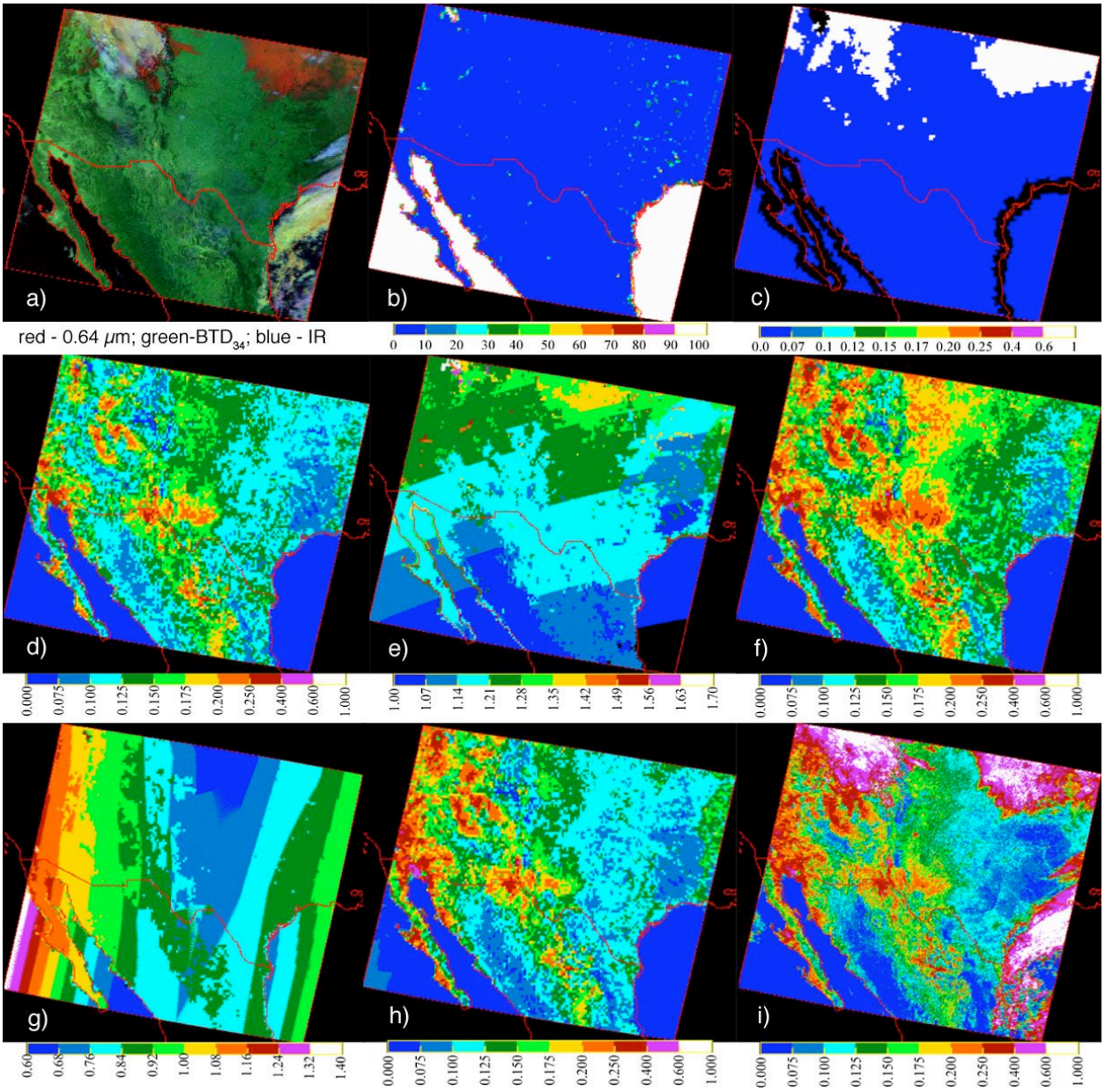

Fig. 10. *Terra* MODIS image and VIS reflectance and mask input and clear-sky VIS parameters, 1700 UTC, 21 December 2000. (a) RGB image, (b) water percentage map, (c) snow-ice map, (d) overhead-sun clear-sky albedo, (e) normalized directional reflectance, (f) clear-sky albedo, (g) BRDF factor, (h) predicted clear-sky reflectance, (i) observed reflectance.

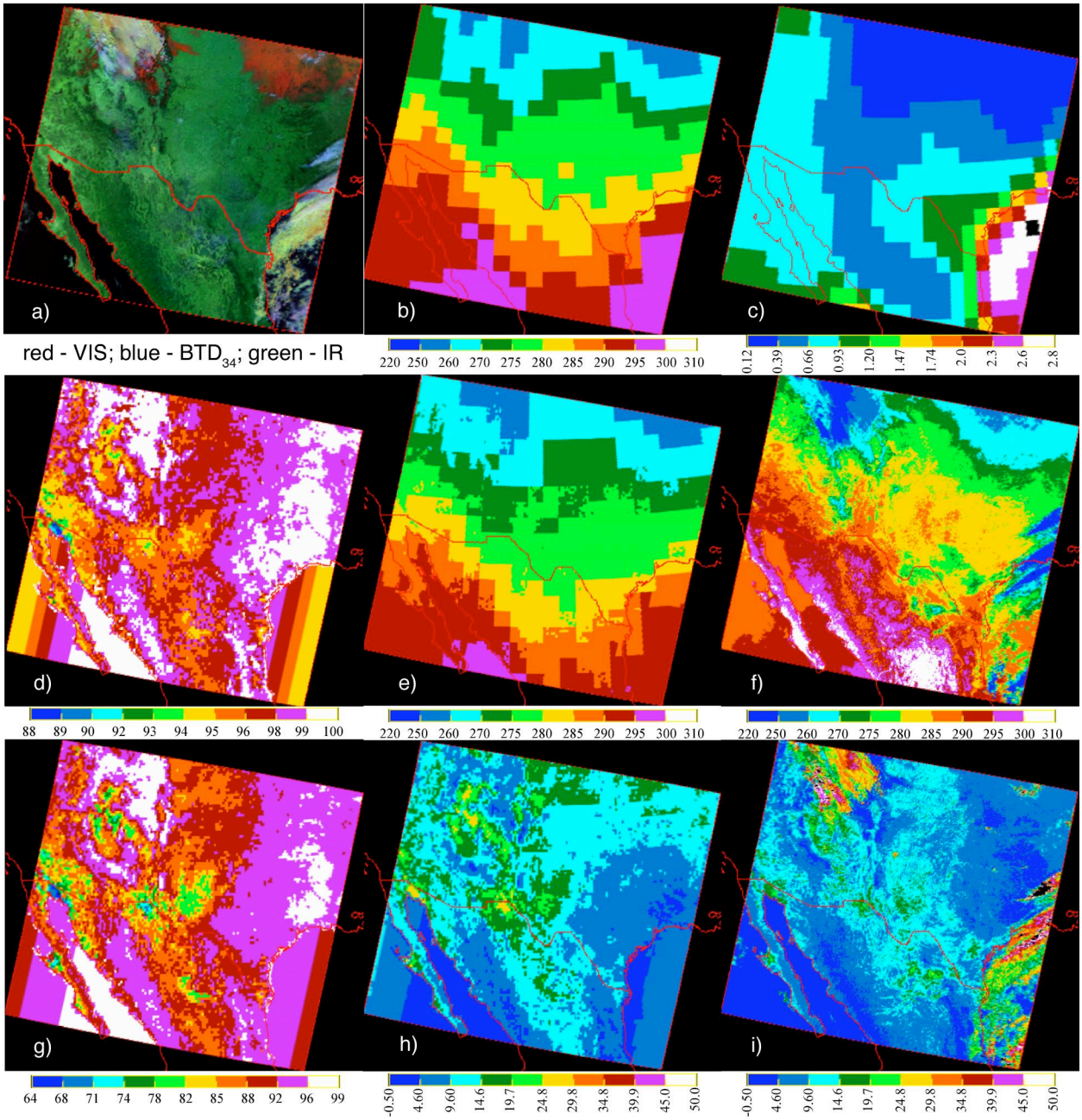

Fig. 11. *Terra* MODIS image, IR temperature, and BTD and mask input and predicted clear-sky IR and BTD parameters, 1700 UTC, 21 December 2000. (a) RGB image, (b) MOA skin temperature, (c) MOA precipitable water vapor in cm, (d) IR surface emissivity, (e) predicted clear-sky IR brightness temperature T_{cs4}, (f) observed IR brightness temperature, (g) 3.8-µm surface emissivity, (h) predicted clear-sky BTD_{cs34}, (i) observed BTD_{34}.

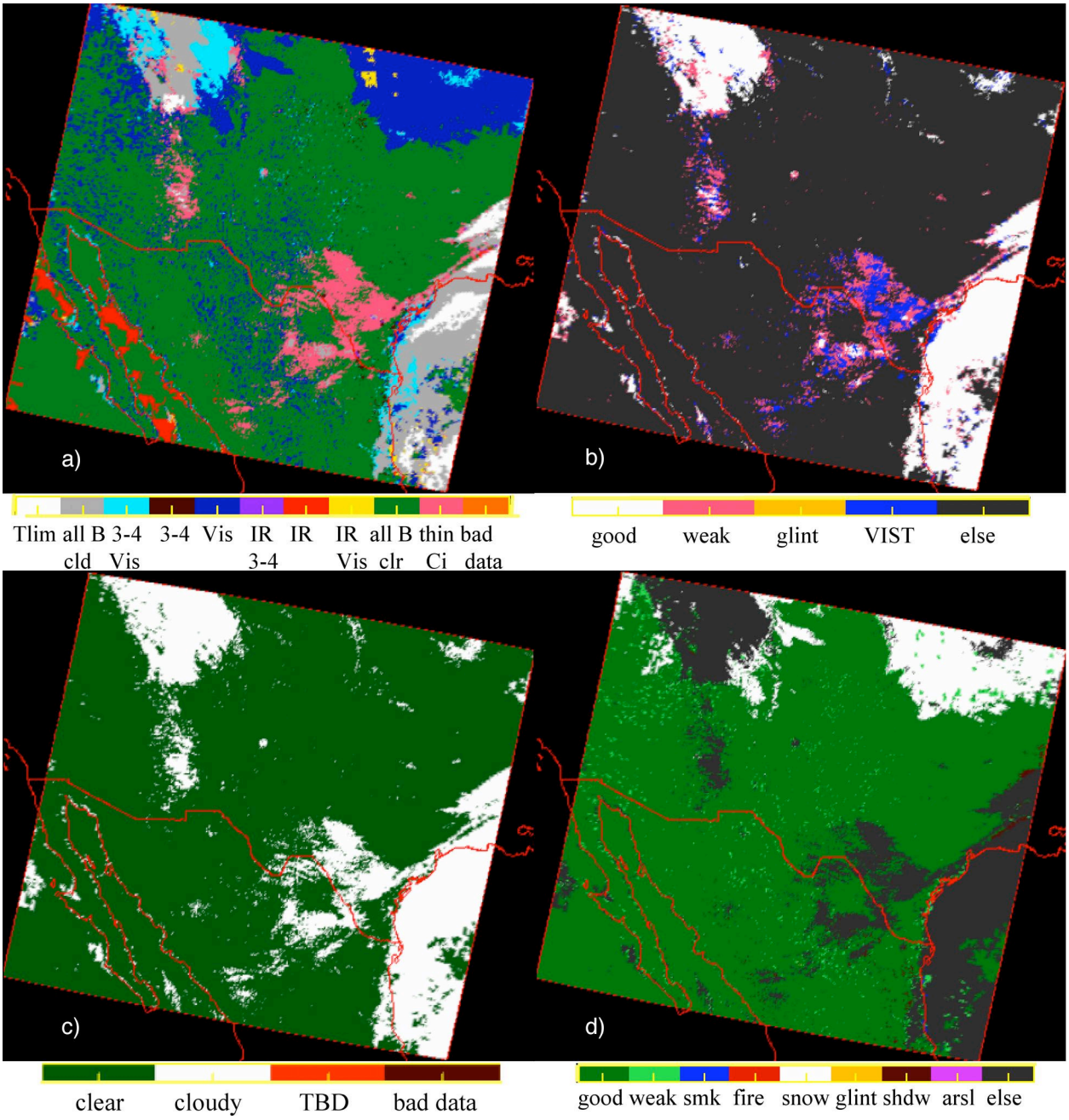

Fig. 12. Pixel classification by CERES daytime non-polar cloud mask for *Terra* MODIS image in Fig. 11a, 1700 UTC, 21 December 2000. (a) final tests used to classify each pixel, (b) cloud quality classification, (c) final cloud mask, (d) final clear-sky classifications.

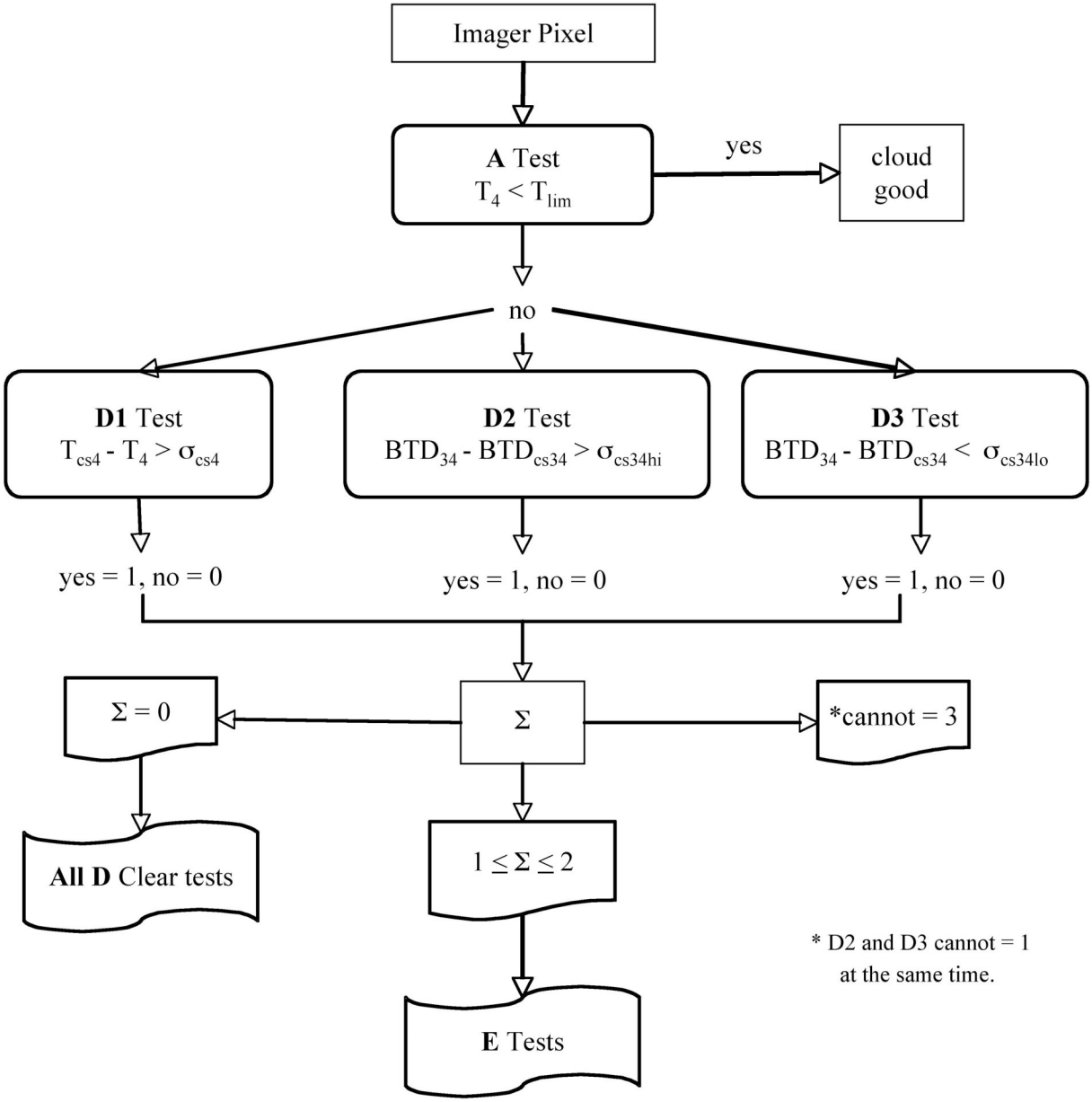

Fig. 13. Schematic diagram of CERES non-polar nighttime scene identification.

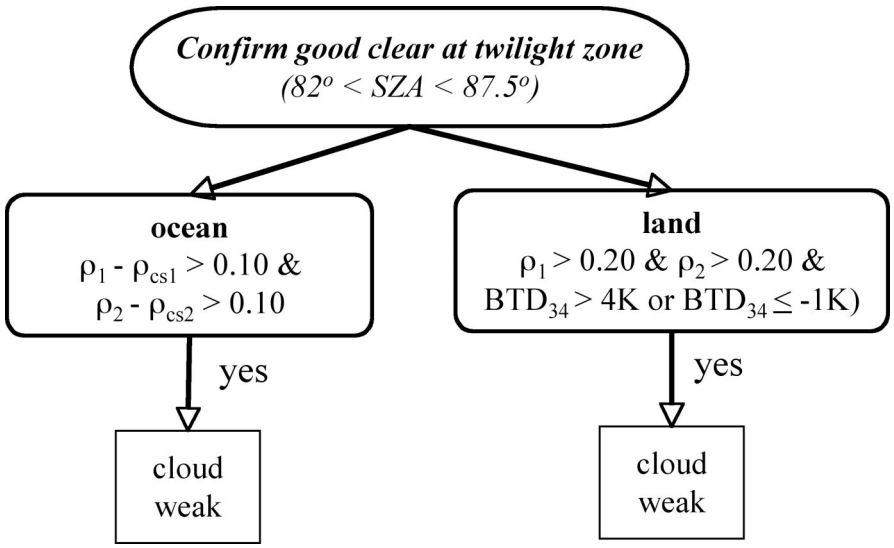

Fig. 14. Flow diagram for twilight tests applied when nighttime mask identifies pixels as good clear and significant sunlight affects the SIR brightness temperature.

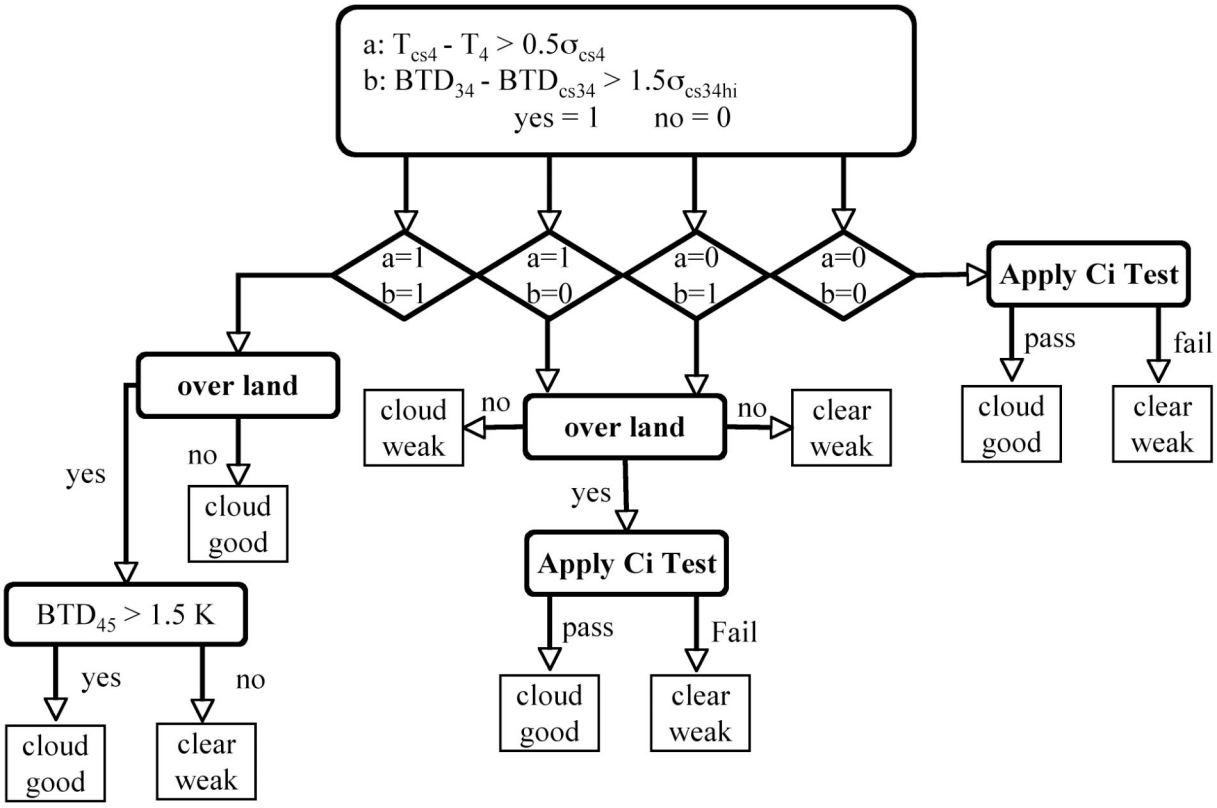

Fig. 15. Nighttime **E1** test applied when *D1* =1, *D2* = 1, and *D3* = 0.

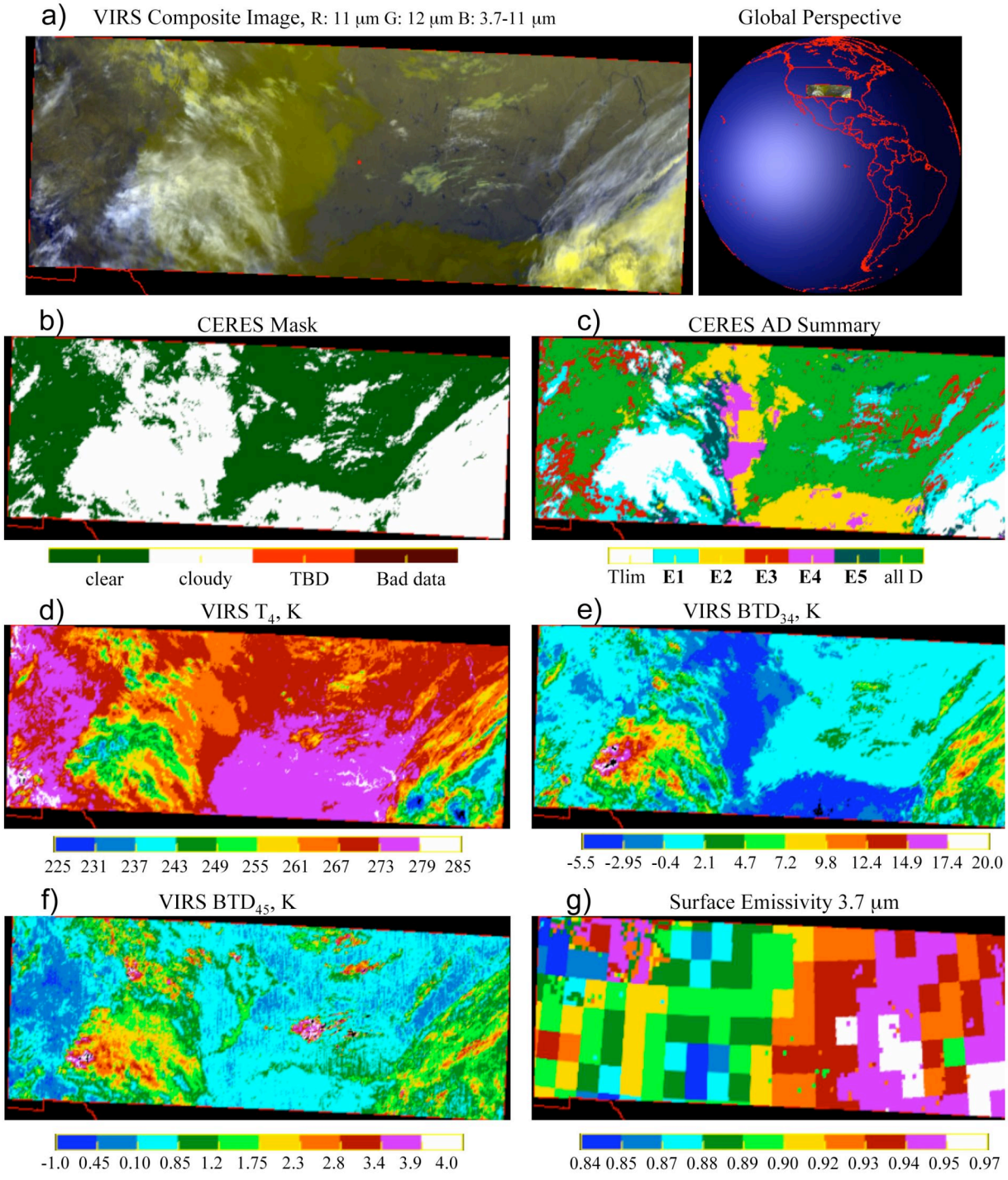

Fig. 16. CERES nocturnal cloud mask for VIRS data taken at 6 UTC, 25 March 2001 over Texas.

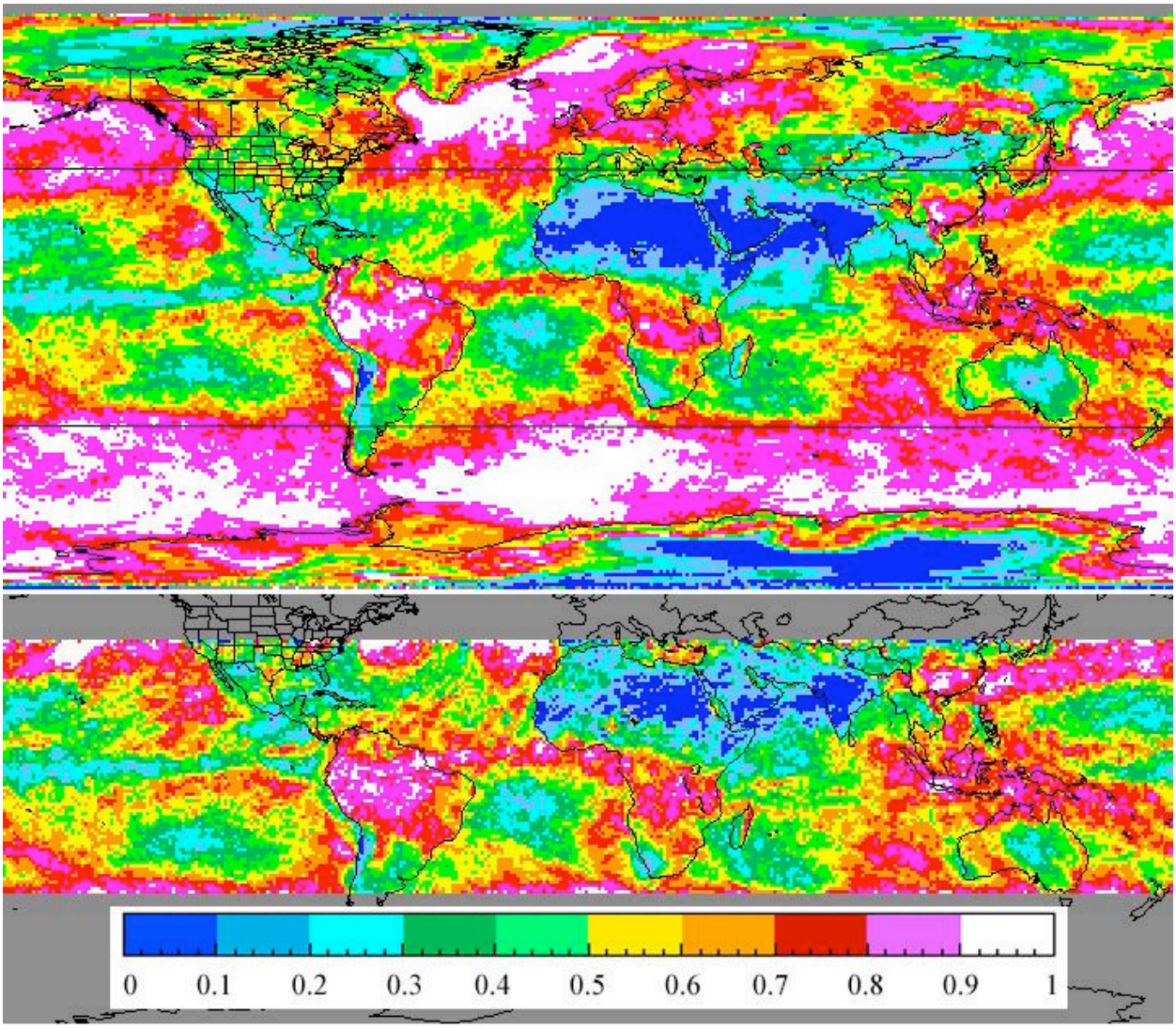

Fig. 17a. Mean CERES daytime cloud amount for March 2000 from (top) *Terra* MODIS and (bottom) TRMM VIRS.

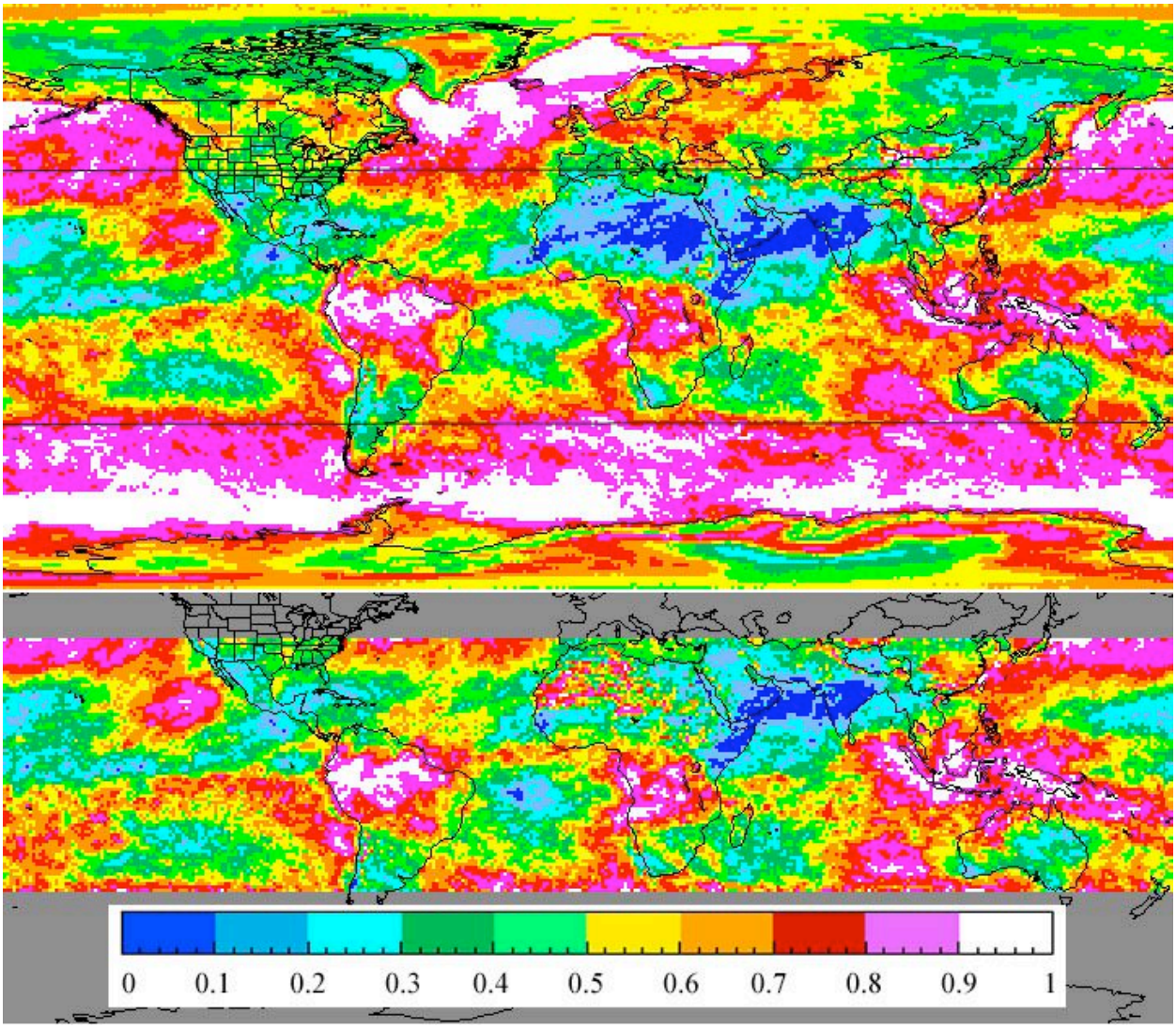

Fig. 17b. Same as Fig. 17a, except for nighttime.

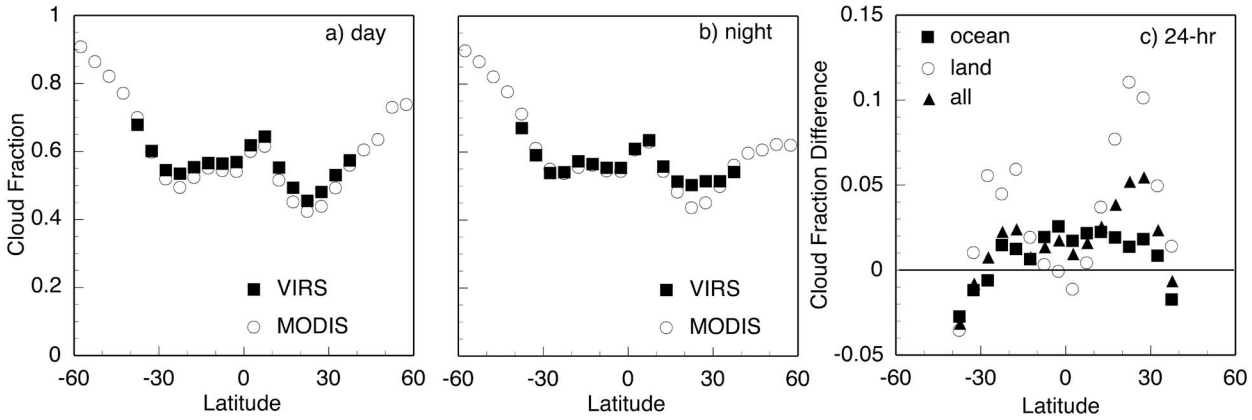

Fig. 18. Mean zonal cloud fraction and differences for summer 2000 (JJA) and winter 2001 (DJF).

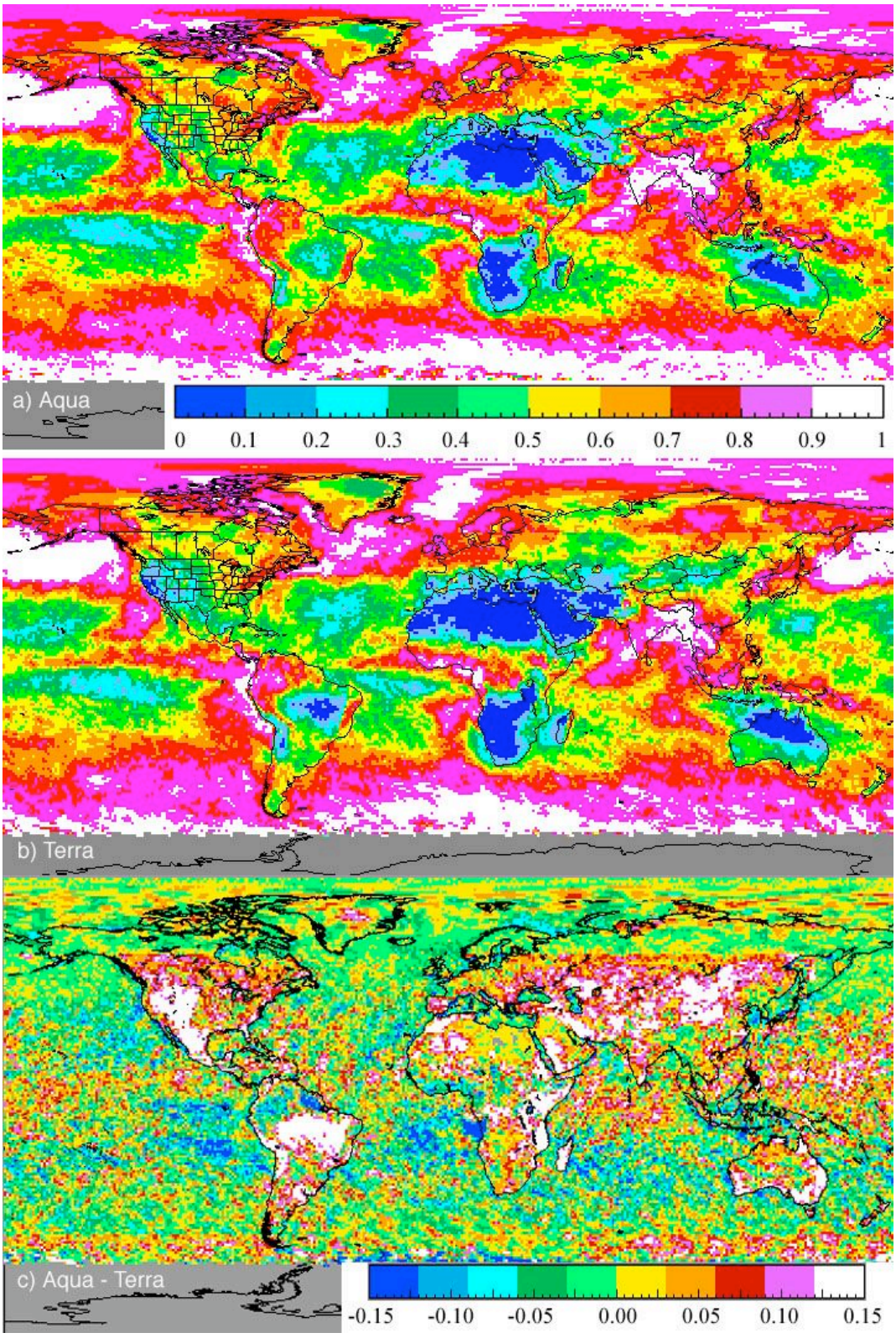

Fig. 19. Mean cloud fraction distributions and differences for July 2004.

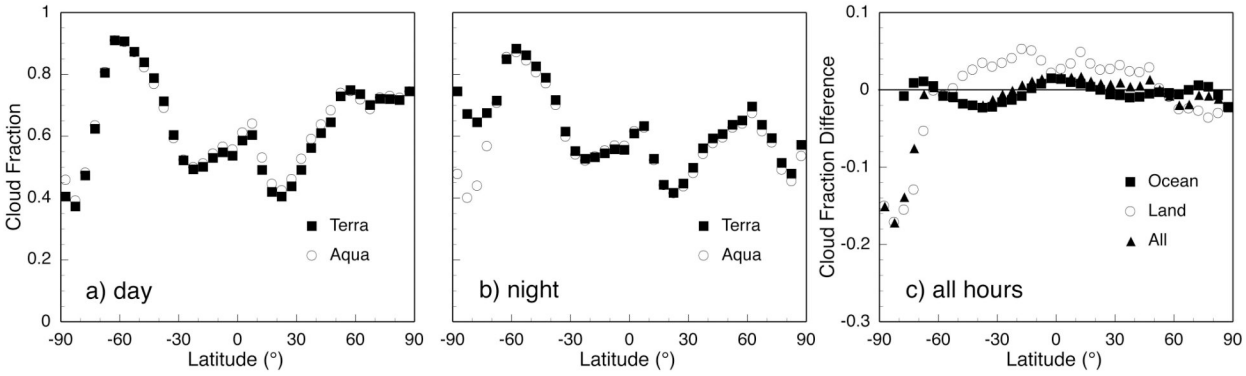

Fig. 20. Mean 2005 CERES zonal cloud fraction and difference.

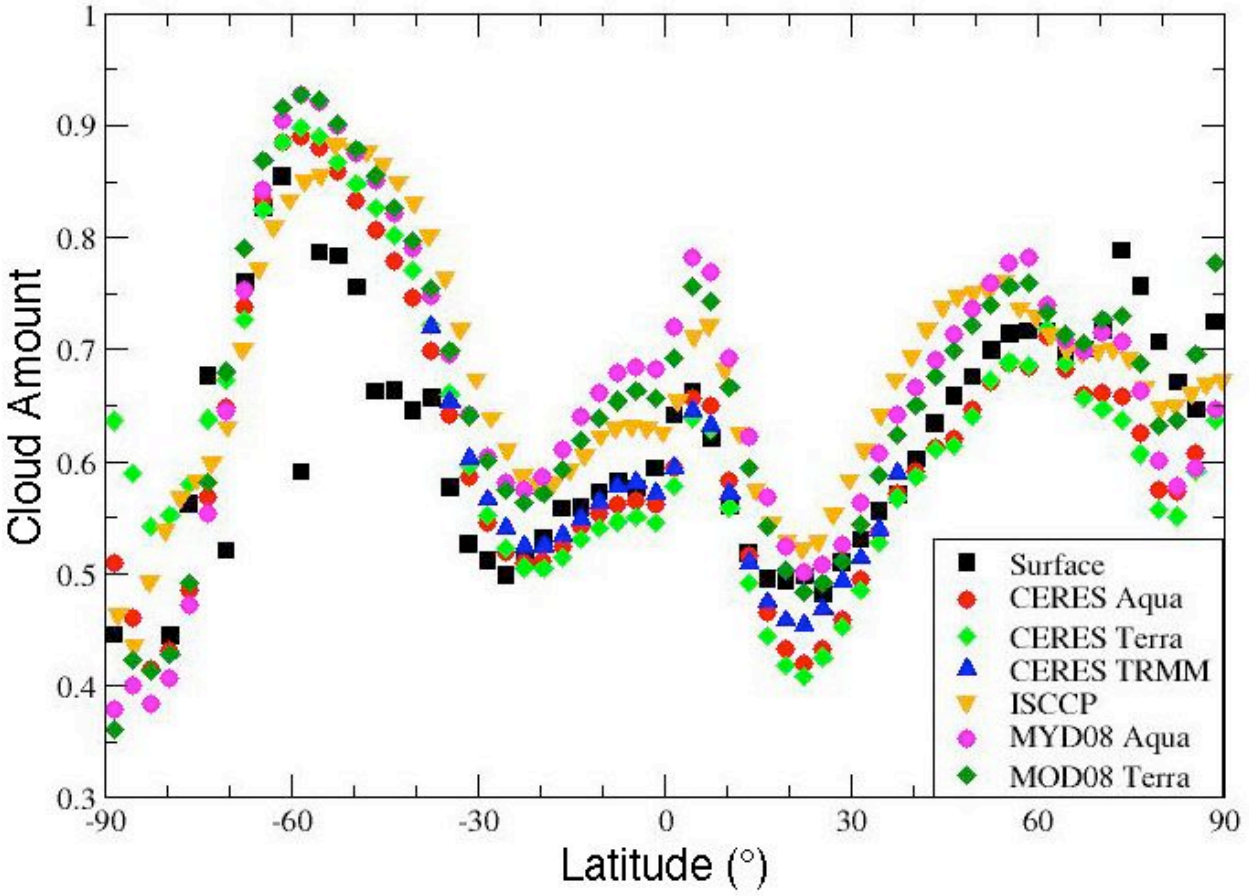

Fig. 21. Mean long-term zonal cloud amounts from several sources. The time periods and averages are listed in Table 6.